

*Fermi* LAT observations of the Geminga pulsar

1  
 2 A. A. Abdo<sup>1,2</sup>, M. Ackermann<sup>3</sup>, M. Ajello<sup>3</sup>, L. Baldini<sup>4</sup>, J. Ballet<sup>5</sup>, G. Barbiellini<sup>6,7</sup>,  
 3 D. Bastieri<sup>8,9</sup>, B. M. Baughman<sup>10</sup>, K. Bechtol<sup>3</sup>, R. Bellazzini<sup>4</sup>, B. Berenji<sup>3</sup>, G. F. Bignami<sup>11</sup>,  
 4 R. D. Blandford<sup>3</sup>, E. D. Bloom<sup>3</sup>, E. Bonamente<sup>12,13</sup>, A. W. Borgland<sup>3</sup>, J. Bregeon<sup>4</sup>,  
 5 A. Brez<sup>4</sup>, M. Brigida<sup>14,15</sup>, P. Bruel<sup>16</sup>, T. H. Burnett<sup>17</sup>, G. A. Caliandro<sup>18</sup>, R. A. Cameron<sup>3</sup>,  
 6 P. A. Caraveo<sup>19</sup>, J. M. Casandjian<sup>5</sup>, C. Cecchi<sup>12,13</sup>, Ö. Çelik<sup>20,21,22</sup>, E. Charles<sup>3</sup>,  
 7 A. Chekhtman<sup>1,23</sup>, C. C. Cheung<sup>1,2</sup>, J. Chiang<sup>3</sup>, S. Ciprini<sup>13</sup>, R. Claus<sup>3</sup>, J. Cohen-Tanugi<sup>24</sup>,  
 8 J. Conrad<sup>25,26,27</sup>, C. D. Dermer<sup>1</sup>, F. de Palma<sup>14,15</sup>, M. Dormody<sup>28</sup>, E. do Couto e Silva<sup>3</sup>,  
 9 P. S. Drell<sup>3</sup>, R. Dubois<sup>3</sup>, D. Dumora<sup>29,30</sup>, Y. Edmonds<sup>3</sup>, C. Farnier<sup>24</sup>, C. Favuzzi<sup>14,15</sup>,  
 10 S. J. Fegan<sup>16</sup>, W. B. Focke<sup>3</sup>, P. Fortin<sup>16</sup>, M. Frailis<sup>31,32</sup>, Y. Fukazawa<sup>33</sup>, S. Funk<sup>3</sup>,  
 11 P. Fusco<sup>14,15</sup>, F. Gargano<sup>15</sup>, D. Gasparrini<sup>34</sup>, N. Gehrels<sup>20</sup>, S. Germani<sup>12,13</sup>, G. Giavitto<sup>6,7</sup>,  
 12 N. Giglietto<sup>14,15</sup>, F. Giordano<sup>14,15</sup>, T. Glanzman<sup>3</sup>, G. Godfrey<sup>3</sup>, I. A. Grenier<sup>5</sup>,  
 13 M.-H. Grondin<sup>29,30</sup>, J. E. Grove<sup>1</sup>, L. Guillemot<sup>35,29,30</sup>, S. Guiriec<sup>36</sup>, D. Hadasch<sup>37</sup>,  
 14 A. K. Harding<sup>20</sup>, E. Hays<sup>20</sup>, R. E. Hughes<sup>10</sup>, G. Jóhannesson<sup>3</sup>, A. S. Johnson<sup>3</sup>,  
 15 T. J. Johnson<sup>20,38</sup>, W. N. Johnson<sup>1</sup>, T. Kamae<sup>3</sup>, H. Katagiri<sup>33</sup>, J. Kataoka<sup>39</sup>, N. Kawai<sup>40,41</sup>,  
 16 M. Kerr<sup>17</sup>, J. Knödseder<sup>42</sup>, M. Kuss<sup>4</sup>, J. Lande<sup>3</sup>, L. Latronico<sup>4</sup>, M. Lemoine-Goumard<sup>29,30</sup>,  
 17 F. Longo<sup>6,7</sup>, F. Loparco<sup>14,15</sup>, B. Lott<sup>29,30</sup>, M. N. Lovellette<sup>1</sup>, P. Lubrano<sup>12,13</sup>, A. Makeev<sup>1,23</sup>,  
 18 M. Marelli<sup>19</sup>, M. N. Mazziotta<sup>15</sup>, J. E. McEnery<sup>20,38</sup>, C. Meurer<sup>25,26</sup>, P. F. Michelson<sup>3</sup>,  
 19 W. Mitthumsiri<sup>3</sup>, T. Mizuno<sup>33</sup>, A. A. Moiseev<sup>21,38</sup>, C. Monte<sup>14,15</sup>, M. E. Monzani<sup>3</sup>,  
 20 A. Morselli<sup>43</sup>, I. V. Moskalenko<sup>3</sup>, S. Murgia<sup>3</sup>, P. L. Nolan<sup>3</sup>, J. P. Norris<sup>44</sup>, E. Nuss<sup>24</sup>,  
 21 T. Ohsugi<sup>45</sup>, N. Omodei<sup>3</sup>, E. Orlando<sup>46</sup>, J. F. Ormes<sup>44</sup>, M. Ozaki<sup>47</sup>, D. Paneque<sup>3</sup>,  
 22 J. H. Panetta<sup>3</sup>, D. Parent<sup>1,23,29,30</sup>, V. Pelassa<sup>24</sup>, M. Pepe<sup>12,13</sup>, M. Pesce-Rollins<sup>4</sup>, F. Piron<sup>24</sup>,  
 23 T. A. Porter<sup>3</sup>, S. Rainò<sup>14,15</sup>, R. Rando<sup>8,9</sup>, P. S. Ray<sup>1</sup>, M. Razzano<sup>4</sup>, A. Reimer<sup>48,3</sup>,  
 24 O. Reimer<sup>48,3</sup>, T. Reposeur<sup>29,30</sup>, L. S. Rochester<sup>3</sup>, A. Y. Rodriguez<sup>18</sup>, R. W. Romani<sup>3</sup>,  
 25 M. Roth<sup>17</sup>, F. Ryde<sup>49,26</sup>, H. F.-W. Sadrozinski<sup>28</sup>, A. Sander<sup>10</sup>, P. M. Saz Parkinson<sup>28</sup>,  
 26 J. D. Scargle<sup>50</sup>, C. Sgrò<sup>4</sup>, E. J. Siskind<sup>51</sup>, D. A. Smith<sup>29,30</sup>, P. D. Smith<sup>10</sup>, G. Spandre<sup>4</sup>,  
 27 P. Spinelli<sup>14,15</sup>, M. S. Strickman<sup>1</sup>, D. J. Suson<sup>52</sup>, H. Takahashi<sup>45</sup>, T. Takahashi<sup>47</sup>,  
 28 T. Tanaka<sup>3</sup>, J. B. Thayer<sup>3</sup>, J. G. Thayer<sup>3</sup>, D. J. Thompson<sup>20</sup>, L. Tibaldo<sup>8,9,5,53</sup>,  
 29 D. F. Torres<sup>37,18</sup>, G. Tosti<sup>12,13</sup>, A. Tramacere<sup>3,54,55</sup>, T. L. Usher<sup>3</sup>, A. Van Etten<sup>3</sup>,  
 30 V. Vasileiou<sup>21,22</sup>, C. Venter<sup>56</sup>, N. Vilchez<sup>42</sup>, V. Vitale<sup>43,57</sup>, A. P. Waite<sup>3</sup>, P. Wang<sup>3</sup>,  
 31 K. Watters<sup>3</sup>, B. L. Winer<sup>10</sup>, K. S. Wood<sup>1</sup>, T. Ylinen<sup>49,58,26</sup>, M. Ziegler<sup>28</sup>

---

<sup>1</sup>Space Science Division, Naval Research Laboratory, Washington, DC 20375, USA

<sup>2</sup>National Research Council Research Associate, National Academy of Sciences, Washington, DC 20001, USA

<sup>3</sup>W. W. Hansen Experimental Physics Laboratory, Kavli Institute for Particle Astrophysics and Cosmology, Department of Physics and SLAC National Accelerator Laboratory, Stanford University, Stanford, CA 94305, USA

<sup>4</sup>Istituto Nazionale di Fisica Nucleare, Sezione di Pisa, I-56127 Pisa, Italy

<sup>5</sup>Laboratoire AIM, CEA-IRFU/CNRS/Université Paris Diderot, Service d’Astrophysique, CEA Saclay, 91191 Gif sur Yvette, France

<sup>6</sup>Istituto Nazionale di Fisica Nucleare, Sezione di Trieste, I-34127 Trieste, Italy

<sup>7</sup>Dipartimento di Fisica, Università di Trieste, I-34127 Trieste, Italy

<sup>8</sup>Istituto Nazionale di Fisica Nucleare, Sezione di Padova, I-35131 Padova, Italy

<sup>9</sup>Dipartimento di Fisica “G. Galilei”, Università di Padova, I-35131 Padova, Italy

<sup>10</sup>Department of Physics, Center for Cosmology and Astro-Particle Physics, The Ohio State University, Columbus, OH 43210, USA

<sup>11</sup>Istituto Universitario di Studi Superiori (IUSS), I-27100 Pavia, Italy

<sup>12</sup>Istituto Nazionale di Fisica Nucleare, Sezione di Perugia, I-06123 Perugia, Italy

<sup>13</sup>Dipartimento di Fisica, Università degli Studi di Perugia, I-06123 Perugia, Italy

<sup>14</sup>Dipartimento di Fisica “M. Merlin” dell’Università e del Politecnico di Bari, I-70126 Bari, Italy

<sup>15</sup>Istituto Nazionale di Fisica Nucleare, Sezione di Bari, 70126 Bari, Italy

<sup>16</sup>Laboratoire Leprince-Ringuet, École polytechnique, CNRS/IN2P3, Palaiseau, France

<sup>17</sup>Department of Physics, University of Washington, Seattle, WA 98195-1560, USA

<sup>18</sup>Institut de Ciències de l’Espai (IEEC-CSIC), Campus UAB, 08193 Barcelona, Spain

<sup>19</sup>INAF-Istituto di Astrofisica Spaziale e Fisica Cosmica, I-20133 Milano, Italy

<sup>20</sup>NASA Goddard Space Flight Center, Greenbelt, MD 20771, USA

<sup>21</sup>Center for Research and Exploration in Space Science and Technology (CRESST) and NASA Goddard Space Flight Center, Greenbelt, MD 20771, USA

<sup>22</sup>Department of Physics and Center for Space Sciences and Technology, University of Maryland Baltimore County, Baltimore, MD 21250, USA

<sup>23</sup>George Mason University, Fairfax, VA 22030, USA

<sup>24</sup>Laboratoire de Physique Théorique et Astroparticules, Université Montpellier 2, CNRS/IN2P3, Montpellier, France

<sup>25</sup>Department of Physics, Stockholm University, AlbaNova, SE-106 91 Stockholm, Sweden

- 
- <sup>26</sup>The Oskar Klein Centre for Cosmoparticle Physics, AlbaNova, SE-106 91 Stockholm, Sweden
- <sup>27</sup>Royal Swedish Academy of Sciences Research Fellow, funded by a grant from the K. A. Wallenberg Foundation
- <sup>28</sup>Santa Cruz Institute for Particle Physics, Department of Physics and Department of Astronomy and Astrophysics, University of California at Santa Cruz, Santa Cruz, CA 95064, USA
- <sup>29</sup>CNRS/IN2P3, Centre d'Études Nucléaires Bordeaux Gradignan, UMR 5797, Gradignan, 33175, France
- <sup>30</sup>Université de Bordeaux, Centre d'Études Nucléaires Bordeaux Gradignan, UMR 5797, Gradignan, 33175, France
- <sup>31</sup>Dipartimento di Fisica, Università di Udine and Istituto Nazionale di Fisica Nucleare, Sezione di Trieste, Gruppo Collegato di Udine, I-33100 Udine, Italy
- <sup>32</sup>Osservatorio Astronomico di Trieste, Istituto Nazionale di Astrofisica, I-34143 Trieste, Italy
- <sup>33</sup>Department of Physical Sciences, Hiroshima University, Higashi-Hiroshima, Hiroshima 739-8526, Japan
- <sup>34</sup>Agenzia Spaziale Italiana (ASI) Science Data Center, I-00044 Frascati (Roma), Italy
- <sup>35</sup>Max-Planck-Institut für Radioastronomie, Auf dem Hügel 69, 53121 Bonn, Germany
- <sup>36</sup>Center for Space Plasma and Aeronomic Research (CSPAR), University of Alabama in Huntsville, Huntsville, AL 35899, USA
- <sup>37</sup>Institució Catalana de Recerca i Estudis Avançats (ICREA), Barcelona, Spain
- <sup>38</sup>Department of Physics and Department of Astronomy, University of Maryland, College Park, MD 20742, USA
- <sup>39</sup>Research Institute for Science and Engineering, Waseda University, 3-4-1, Okubo, Shinjuku, Tokyo, 169-8555 Japan
- <sup>40</sup>Department of Physics, Tokyo Institute of Technology, Meguro City, Tokyo 152-8551, Japan
- <sup>41</sup>Cosmic Radiation Laboratory, Institute of Physical and Chemical Research (RIKEN), Wako, Saitama 351-0198, Japan
- <sup>42</sup>Centre d'Étude Spatiale des Rayonnements, CNRS/UPS, BP 44346, F-30128 Toulouse Cedex 4, France
- <sup>43</sup>Istituto Nazionale di Fisica Nucleare, Sezione di Roma "Tor Vergata", I-00133 Roma, Italy
- <sup>44</sup>Department of Physics and Astronomy, University of Denver, Denver, CO 80208, USA
- <sup>45</sup>Hiroshima Astrophysical Science Center, Hiroshima University, Higashi-Hiroshima, Hiroshima 739-8526, Japan
- <sup>46</sup>Max-Planck Institut für extraterrestrische Physik, 85748 Garching, Germany
- <sup>47</sup>Institute of Space and Astronautical Science, JAXA, 3-1-1 Yoshinodai, Sagamihara, Kanagawa 229-8510, Japan
- <sup>48</sup>Institut für Astro- und Teilchenphysik and Institut für Theoretische Physik, Leopold-Franzens-

**ABSTRACT**

32

33

We report on the *Fermi*-LAT observations of the Geminga pulsar, the second brightest non-variable GeV source in the  $\gamma$ -ray sky and the first example of a radio-quiet  $\gamma$ -ray pulsar. The observations cover one year, from the launch of the *Fermi* satellite through 2009 June 15. A data sample of over 60,000 photons enabled us to build a timing solution based solely on  $\gamma$  rays. Timing analysis shows two prominent peaks, separated by  $\Delta\phi = 0.497 \pm 0.004$  in phase, which narrow with increasing energy. Pulsed  $\gamma$  rays are observed beyond 18 GeV, precluding emission below 2.7 stellar radii because of magnetic absorption. The phase-averaged spectrum was fitted with a power law with exponential cut-off of spectral index  $\Gamma = (1.30 \pm 0.01 \pm 0.04)$ , cut-off energy  $E_0 = (2.46 \pm 0.04 \pm 0.17)$  GeV and an integral photon flux above 0.1 GeV of  $(4.14 \pm 0.02 \pm 0.32) \times 10^{-6} \text{ cm}^{-2} \text{ s}^{-1}$ . The first uncertainties are statistical and the second are systematic. The phase-resolved spectroscopy shows a clear evolution of the spectral parameters, with the spectral index reaching a minimum value just before the leading peak and the cut-off energy having maxima around the peaks. Phase-resolved spectroscopy reveals that pulsar emission is present at all rotational phases. The spectral shape, broad pulse profile, and maximum photon energy favor the outer magnetospheric emission scenarios.

34

*Subject headings:* gamma rays: observations; pulsars: general; pulsars: individual (PSR J0633+1746, Geminga)

35

---

Universität Innsbruck, A-6020 Innsbruck, Austria

<sup>49</sup>Department of Physics, Royal Institute of Technology (KTH), AlbaNova, SE-106 91 Stockholm, Sweden

<sup>50</sup>Space Sciences Division, NASA Ames Research Center, Moffett Field, CA 94035-1000, USA

<sup>51</sup>NYCB Real-Time Computing Inc., Lattingtown, NY 11560-1025, USA

<sup>52</sup>Department of Chemistry and Physics, Purdue University Calumet, Hammond, IN 46323-2094, USA

<sup>53</sup>Partially supported by the International Doctorate on Astroparticle Physics (IDAPP) program

<sup>54</sup>Consorzio Interuniversitario per la Fisica Spaziale (CIFS), I-10133 Torino, Italy

<sup>55</sup>INTEGRAL Science Data Centre, CH-1290 Versoix, Switzerland

<sup>56</sup>North-West University, Potchefstroom Campus, Potchefstroom 2520, South Africa

<sup>57</sup>Dipartimento di Fisica, Università di Roma “Tor Vergata”, I-00133 Roma, Italy

<sup>58</sup>School of Pure and Applied Natural Sciences, University of Kalmar, SE-391 82 Kalmar, Sweden

## 1. Introduction

36

37 The Geminga pulsar is the second brightest non-variable GeV  $\gamma$ -ray source in the sky  
 38 and the first representative of a population of radio-quiet  $\gamma$ -ray pulsars. Since its discovery  
 39 as a  $\gamma$ -ray source by SAS-2, more than thirty years ago (Fichtel et al. 1975; Kniffen et al.  
 40 1975), Geminga has been alternatively considered as a unique object or as the prototype of  
 41 a population of hidden dead stars. *Fermi* has now settled this question with the discovery  
 42 (Abdo et al. 2009g) of a substantial population of potentially radio-quiet pulsars, of which  
 43 Geminga was indeed the harbinger.

44 Geminga was then observed by the COS B  $\gamma$ -ray telescope (Bennett et al. 1977; Masnou et al.  
 45 1981), appearing as 2CG 195+04 in the second COS B catalog (Swanenburg et al. 1981)  
 46 and eventually acquiring the name Geminga (Bignami et al. 1983). The X-ray source 1E  
 47 0630+178 detected by the *Einstein Observatory* in the COS B error box (Bignami et al.  
 48 1983) was proposed as a possible counterpart, and subsequently an optical candidate was  
 49 found within the *Einstein* error box (Bignami et al. 1987), which was the bluest object in  
 50 the field (Halpern & Tytler 1988; Bignami et al. 1988).

51 The subsequent ROSAT detection of periodic X-rays from this source (Halpern & Holt  
 52 1992) prompted a successful search for periodicity in high-energy  $\gamma$  rays with EGRET  
 53 (Bertsch et al. 1992).

54 Geminga has a period of 237 ms and a very stable period derivative of  $1.1 \times 10^{-14} \text{ s s}^{-1}$ ,  
 55 that characterize it as a mature pulsar with characteristic age of  $3 \times 10^5 \text{ yr}$  and spin-down  
 56 luminosity  $\dot{E} = 3.26 \times 10^{34} \text{ erg s}^{-1}$ .

57 The determination of the period derivative allowed detection of  $\gamma$ -ray pulsations in the  
 58 previous COS B (Bignami & Caraveo 1992) and SAS-2 data (Mattox et al. 1992). Mean-  
 59 while, a high proper motion of 170 mas/yr for the faint  $m_V = 25.5$  optical counterpart was  
 60 found, confirming the object to be both underluminous and no more than few hundred pc  
 61 away (Bignami et al. 1993). Using HST, Caraveo et al. (1996) obtained a parallax distance  
 62 for Geminga of  $157_{-34}^{+59} \text{ pc}$ . A comprehensive review of the history of the identification of  
 63 Geminga can be found in Bignami & Caraveo (1996).

64 Subsequently, high resolution astrometry with the *Hipparcos* mission allowed for a 40 mas  
 65 absolute positioning of Geminga (Caraveo et al. 1998). Such accurate positioning, together  
 66 with the source proper motion, was used by Mattox et al. (1998) to improve the quality of  
 67 the timing solution of the pulsar. Recent parallax and proper motion measurements confirm  
 68 the earlier results, yielding a distance of  $250_{-62}^{+120} \text{ pc}$  and a proper motion of  $178.2 \pm 0.4$   
 69 mas/yr (Faherty et al. 2007).

70 Analysis of EGRET data showed a double peaked light curve with a peak separation of  $\sim 0.5$   
 71 in phase (Mayer-Hasselwander et al. 1994; Fierro et al. 1998). The Geminga spectrum mea-  
 72 sured by EGRET was compatible with a power law with a falloff at  $\sim 2 \text{ GeV}$ , but the limited

73 EGRET statistics did not allow a measurement of the cut-off energy. Deep X-ray observations  
 74 allowed *XMM-Newton* and *Chandra* to map the neutron star surface as it rotates, bringing  
 75 into view different regions contributing different spectral components (Caraveo et al. 2004;  
 76 De Luca et al. 2005; Jackson & Halpern 2005) as well as an arcmin-scale bow-shock feature  
 77 trailing the pulsar’s motion (Caraveo et al. 2003; De Luca et al. 2006). A synchrotron ori-  
 78 gin of such a non-thermal diffuse X-ray emission trailing the pulsar implies the presence of  
 79 high-energy electrons ( $E > 10^{14}$  eV, a value close to the upper energy limit for pulsar wind  
 80 electrons in Geminga) diffusing in a  $10 \mu\text{G}$  magnetic field.  
 81 Even though Geminga has been one of the most intensively studied isolated neutron stars  
 82 during the last thirty years, it remains of current interest, especially at  $\gamma$ -ray energies where  
 83 its narrow-peaked light curve allows precise timing studies. Thus, it comes as no surprise  
 84 that Geminga has been a prime target for the  $\gamma$ -ray instruments currently in operation:  
 85 AGILE (Tavani et al. 2009) and the Large Area Telescope (LAT) on the *Fermi* mission  
 86 (Atwood et al. 2009). Following its launch, the LAT was confirmed to be an excellent instru-  
 87 ment for pulsar studies, observing the bright Vela pulsar (Abdo et al. 2009a) and discovering  
 88 a variety of new  $\gamma$ -ray pulsars (Abdo et al. 2009b,c,d,e), including millisecond  $\gamma$ -ray pulsars  
 89 (Abdo et al. 2009f) and a population of Geminga-like pulsars detected with blind search  
 90 techniques (Abdo et al. 2009g). In this Paper we present the analysis of the Geminga pulsar  
 91 based on the excellent statistics collected during the first year of operations of the *Fermi*  
 92 mission.

## 93 2. $\gamma$ -ray observations

94 The Large Area Telescope (LAT) aboard *Fermi* is an electron-positron pair conversion  
 95 telescope sensitive to  $\gamma$  rays of energies from 20 MeV to  $> 300$  GeV. The LAT is made of  
 96 a high-resolution silicon microstrip tracker, a CsI hodoscopic electromagnetic calorimeter  
 97 and an Anticoincidence detector for charged particles background identification. The full  
 98 description of the instrument and its performance can be found in Atwood et al. (2009).  
 99 The LAT has a large effective area (peaking at  $\sim 8000$  cm<sup>2</sup> on axis) and thanks to its field of  
 100 view ( $\sim 2.4$  sr) covers the entire sky every 2 orbits ( $\sim 3$  h). The LAT point spread function  
 101 (PSF) strongly depends on both the energy and the conversion point in the tracker, but less  
 102 on the incidence angle. For 1 GeV normal incidence conversions in the upper section of the  
 103 tracker the PSF 68% containment radius is  $0.6^\circ$ .  
 104 The data used in this Paper span roughly the first year of operations after the launch of  
 105 *Fermi* on 2008 June 11. The data used for the timing analysis encompass the *Launch and*  
 106 *Early Operations* (L&EO), covering  $\sim$  two months after 2008 June 25, when the LAT was  
 107 operated in pointing and scanning mode for check-out and calibration purposes, and extend

108 into the first year of nominal operations up to 2009 June 15. For the spectral analysis we  
 109 selected only data collected in scanning mode, under nominal configuration, from 2008 Au-  
 110 gust 4 to 2009 June 15. We selected photons in the ‘diffuse’ event class (lowest background  
 111 contamination, see Atwood et al. 2009) and we excluded observations when Geminga was  
 112 viewed at zenith angles  $> 105^\circ$  where Earth’s albedo  $\gamma$ -rays increase the background contam-  
 113 ination. We also excluded time intervals when the  $15^\circ$  Region Of Interest (ROI) intersects  
 114 the Earth’s albedo region.

### 115 3. Timing Geminga using $\gamma$ rays

116 Since the end of the EGRET mission, the Geminga timing ephemeris has been main-  
 117 tained using occasional observations with *XMM-Newton* (Jackson & Halpern 2005; J. Halpern,  
 118 private communication). While AGILE relied on such X-ray ephemerides (Pellizzoni et al.  
 119 2009), LAT densely-sampled, high-precision timing observations yielded an independent tim-  
 120 ing solution. In fact, the LAT timing is derived from a GPS clock on the spacecraft and times  
 121 of arrival of  $\gamma$  rays are recorded with an accuracy significantly better than  $1 \mu\text{s}$  (Abdo et al.  
 122 2009h). We have constructed a timing solution for Geminga using the *Fermi* LAT data, ex-  
 123 clusively. For this analysis, we assumed a constant location for the Geminga pulsar calculated  
 124 at the center of the time span of the LAT data set (MJD 54800) using the position reported  
 125 by Caraveo et al. (1998) and updated according to the source proper motion (Faherty et al.  
 126 2007).

127 We determined an initial, approximate, ephemeris using an epoch-folding search. We then  
 128 measured pulse times-of-arrival (TOAs) by first converting the photon event times to a ref-  
 129 erence point at the geocenter using the *Fermi* science tool<sup>1</sup> *gtbary*, then computing a pulse  
 130 profile using phases generated using TEMPO2 (Hobbs et al. 2006) in its predictive mode.  
 131 The timing accuracy of *gtbary* was demonstrated in Smith et al. (2008). This was done with  
 132  $\sim 22$  day segments of data. TOAs were determined from each segment using a Fourier-  
 133 domain cross correlation with a high signal-to-noise template profile. We obtained 16 TOAs  
 134 in this way from 2008 June 25 to 2009 June 15. We fit these TOAs, again using TEMPO2,  
 135 to a model with only absolute phase, frequency and frequency first derivative as free param-  
 136 eters. The residuals to the model have an RMS of  $251 \mu\text{s}$ , as shown in Figure 1, and the  
 137 model parameters are listed in Table 1. The epoch of phase 0.0 given in Table 1 is defined so  
 138 that the phase of the first component of the Fourier transform of the light curve has 0 phase.  
 139 However, in order to assign a smaller phase to the leading peak, we introduced an additional  
 140 phase shift of 0.5 to the timing solution in Table 1. Thus, in the light curve shown in Figure

---

<sup>1</sup><http://fermi.gsfc.nasa.gov/ssc/data/analysis/scitools/overview.html>

141 2, the epoch of phase 0.0 is the barycentric arrival time MJD(TDB) corresponding to phase  
 142 0.5.

Table 1: *Fermi*-LAT Ephemeris for Geminga

Parameter	Value
Epoch of position (MJD)	54800
R.A. (J2000)	6:33:54.289
Dec. (J2000)	+17:46:14.38
Epoch of ephemeris $T_0$ (MJD)	54800
Range of valid dates (MJD)	54642 – 54975
Frequency $f$ ( $s^{-1}$ )	4.21756706493(4)
Freq. derivative $\dot{f}$ ( $\times 10^{-13} s^{-2}$ )	-1.95250(9)
Freq. 2nd derivative $\ddot{f}$ ( $s^{-3}$ )	0
Epoch of Phase 0.0 (MJD(TDB))	54819.843013078(3)
Time Units	TDB

143

## 144 4. Results

### 145 4.1. Light curves

146 The strong energy dependence of the PSF imposes energy-dependent regions of interest  
 147 (ROI) that optimize the signal to noise ratio. Following a procedure similar to that used for  
 148 the *Fermi*-LAT pulsar catalogue paper (Abdo et al. 2009l), to study the pulse profiles we  
 149 selected photons within an angle  $\theta < \max[1.6-3\log_{10}(E_{GeV}), 1.3]$  degrees from Geminga. Such  
 150 selection provides clean light curves by limiting acceptance of the softer Galactic background.

151 We used the *Fermi* tool *gtpphase* to correct photon arrival times to the Solar System  
 152 barycenter using the JPL DE405 Solar System ephemeris (Standish 1998) and to assign a  
 153 rotational phase to each photon using the timing solution described in Section 3.  
 154 Figure 2 shows the light curve of Geminga above 0.1 GeV obtained with the energy-dependent  
 155 cut. In order to better show the fine structure, we plot the pulse profile using variable-width  
 156 phase bins, each one containing 400 events. The photon flux in each phase interval thus  
 157 has a  $1\sigma$  Poisson statistical error of 5%. The dashed line represents the contribution of the  
 158 diffuse background, estimated by selecting photons in the phase interval  $\phi = 0.9-1.0$  from an  
 159 annular region between  $2^\circ$  and  $3^\circ$  from the source rescaled for the solid angle and also taking  
 160 into account the energy-dependent selection adopted. The light curve contains  $61219 \pm 284$



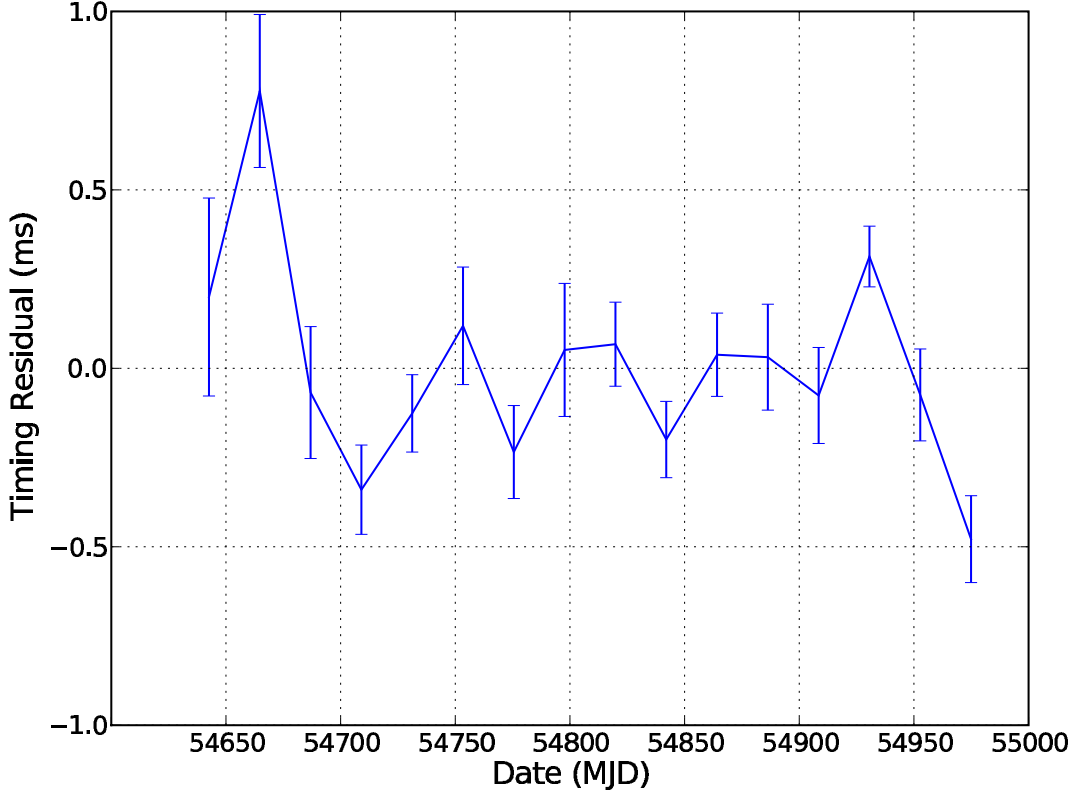


Fig. 1.— Timing residuals of Geminga derived from the model built using the TOAs of the  $\gamma$  rays detected by the LAT (See Section 3 for details).

161 pulsed photons and  $9821 \pm 99$  background photons.  
 162 The pulse profile shows two clear peaks at  $\phi = 0.141 \pm 0.002$  (P1) and  $\phi = 0.638 \pm 0.003$   
 163 (P2). In order to reveal possible asymmetries in the peaks, we started by fitting the sharp  
 164 peaks with two half-Lorentzian profiles with different widths for the trailing and the leading  
 165 edge. We have chosen this function because it has a simple parameterization and appear  
 166 to fit well the pulse profile of the gamma-ray light curves. We found that Geminga peaks  
 167 show no asymmetries, and P1 is broader (FWHM of  $0.072 \pm 0.002$ ) than P2 (FWHM  $0.061$   
 168  $\pm 0.001$ ). We also checked if the peaks can be better fitted by a Gaussian profile, finding  
 169 comparable results (P1 FWHM of  $0.071 \pm 0.002$ ) and (P1 FWHM of  $0.063 \pm 0.001$ ), though  
 170 we cannot distinguish between a Lorentz or Gaussian profile. The smallest features in the  
 171 pulse profile appear on a scale of  $260 \mu\text{s}$ , presumably artifacts of the timing model residuals.  
 172 Figure 2 also contains insets (binned to 0.00125 in phase) centered on the two peaks and on

173 the phase interval  $\phi = 0.9\text{--}1.0$ . This off-peak, or “second interpeak”, region contains  $789 \pm$   
 174  $28$  pulsed photons above the estimated background ( $\sim 1.3 \times 10^{-2}$  of the pulsed flux). This  
 175 corresponds to a signal-to-noise ratio of  $19\sigma$ , indicating that the pulsar emission extends also  
 176 in the off-peak, as will be investigated further in Section 4.3.

Figure 3 shows the pulse profile in five energy ranges (0.1–0.3 GeV, 0.3–1 GeV, 1–3 GeV,

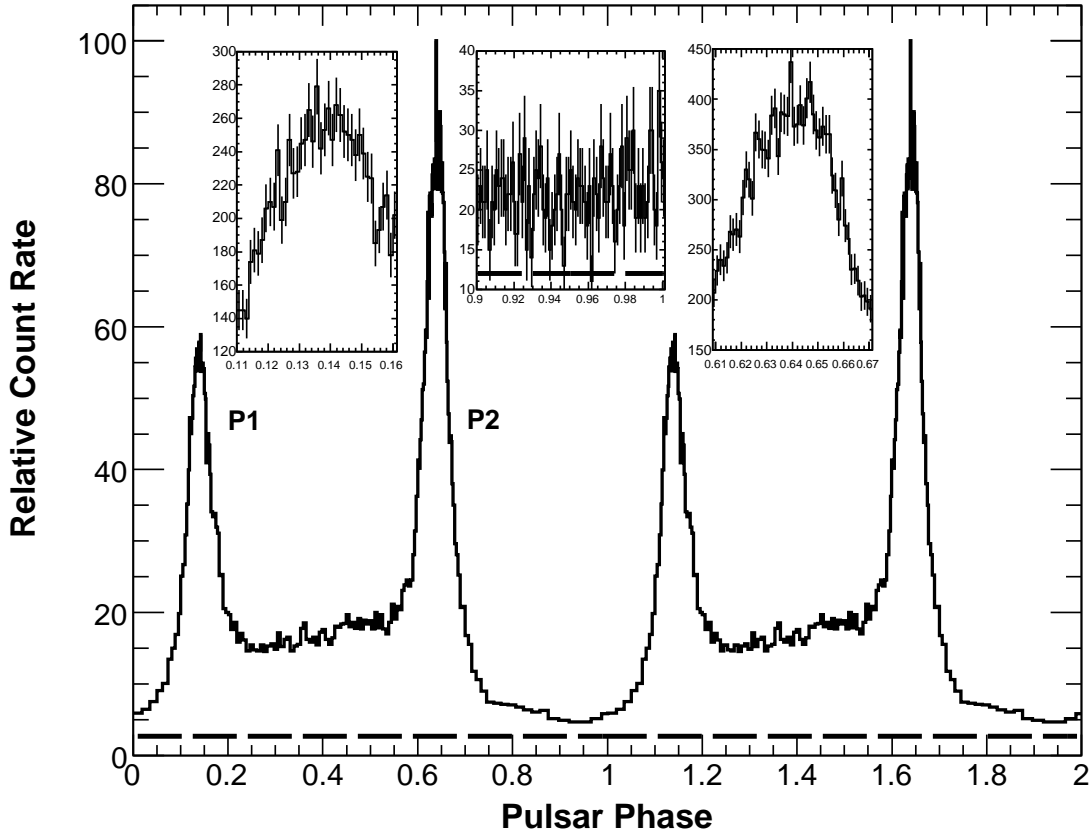


Fig. 2.— Geminga light curve above 0.1 GeV using an energy-dependent ROI, shown over two pulse periods. The count rate is shown in variable-width bins, each one containing 400 counts per bin and normalized to 100. Insets show the phase intervals centered on the two peaks and on the “second interpeak” region ( $\phi = 0.9\text{--}1.0$ ), binned to 0.00125 in phase. The dashed line represents the contribution of the diffuse background estimated by selecting photons in this “second interpeak” interval in an annulus around the source.

177

178 3–10 GeV,  $> 10$  GeV). There is a clear evolution of the light curve shape with energy:  
 179 P1 becomes weaker with increasing energy, while P2 is still detectable at high energies.  
 180 Significant pulsations from P2 are detectable at energies beyond  $\epsilon_{max} \sim 18$  GeV, chosen as

181 the maximum energy beyond which a  $\chi^2$  periodicity test still attains  $6\sigma$  significance. We  
 182 detect 16 photons above 18 GeV, not necessarily coming from the pulsar itself. No particular  
 183 features appear at high energies in the bridge region between P1 and P2 (“first interpeak”).  
 184 Figure 4 shows the evolution of the P1/P2 ratio as a function of energy, plotted using  
 185 variable-width energy bins. The curve depends very weakly on the bin choice, Figure 4 was  
 186 made using 10000 events per bin. A clear decreasing trend is visible, as observed in Crab, Vela  
 187 and PSR B1951+32  $\gamma$ -ray pulsars by EGRET (Thompson 2004) and now confirmed for the  
 188 Vela (Abdo et al. 2009a) and the Crab pulsars (Abdo et al. 2010c) by *Fermi* LAT. Adopting  
 189 the same variable-width energy bins we fit the peaks in each energy range with a Lorentz  
 190 function to determine the peak center and width. Figure 5 shows the energy evolution of  
 191 the FWHM of P1 and P2: both peaks narrow with increasing energy. The decreasing trend  
 192 in pulse width of P1 and P2 is nearly identical. P1 has a FWHM decreasing from  $\delta\phi =$   
 193  $0.098 \pm 0.004$  to  $\delta\phi = 0.053 \pm 0.008$ , while FWHM of P2 changes from  $\delta\phi = 0.092 \pm 0.004$   
 194 to  $\delta\phi = 0.044 \pm 0.004$  at energies greater than 3 GeV. The decrease in width with energy  
 195 does not depend on the shape used to fit the peaks. Figure 8 was made using the Lorentzian  
 196 fits, preferred in general because sensitive to asymmetric pulses. While the “first interpeak”  
 197 emission is significantly detected up to 10 GeV, emission in the “second interpeak” region  
 198 (between 0.9 and 1.0), not detected before, is clearly present at low energies but vanishes  
 199 above  $\sim 2$  GeV.

200

## 201 4.2. Energy Spectrum

202 Spectral analysis was performed using the maximum-likelihood estimator *glike* included  
 203 in the standard *Fermi* Science Tools provided by the FSSC. The fit was performed using a  
 204 region of the sky with a radius of  $15^\circ$  around the pulsar position selecting energies between  
 205 0.1 and 100 GeV.

206 We included in the fit a model accounting for the diffuse emission as well as for the nearby  
 207  $\gamma$ -ray sources. We modeled the diffuse foreground, including Galactic interstellar emission,  
 208 extragalactic  $\gamma$ -ray emission and residual CR background, using the models<sup>2</sup> *gll\_iem\_v02* for  
 209 the Galactic part and *isotropic\_iem\_v02* for the isotropic one.

210 In the fit procedure we fixed the spectral parameters of all the sources between  $15^\circ$  and  $20^\circ$   
 211 from Geminga, and left free the normalization factor of all the sources within  $15^\circ$ . All the  
 212 non-pulsar sources have been modeled with a power law as reported in the *Fermi* Bright  
 213 Source List (Abdo et al. 2009l), while all the pulsars have been described by a power law

---

<sup>2</sup><http://fermi.gsfc.nasa.gov/ssc/data/access/lat/BackgroundModels.html>

214 with exponential cut-off according to the data reported in the *Fermi*-LAT pulsar catalogue  
 215 (Abdo et al. 2009l).

216 We integrated the phase-averaged spectrum to obtain the energy flux. The unbinned *gtlike*  
 217 fit is described by a power law with exponential cut-off in the form:

$$\frac{dN}{dE} = N_0 E^{-\Gamma} \exp\left(-\frac{E}{E_0}\right) \text{cm}^{-2} \text{s}^{-1} \text{GeV}^{-1} \quad (1)$$

218 where  $N_0 = (1.189 \pm 0.013 \pm 0.070) \times 10^{-9} \text{cm}^{-2} \text{s}^{-1} \text{GeV}^{-1}$ ,  $\Gamma = (1.30 \pm 0.01 \pm 0.04)$   
 219 and  $E_0 = (2.46 \pm 0.04 \pm 0.17) \text{GeV}$ . The first uncertainties are statistical values for the fit  
 220 parameters, while the second ones are systematic uncertainties. Systematics are mainly based  
 221 on uncertainties on the LAT effective area derived from the on-orbit estimations, and are of  
 222  $\leq 5\%$  near 1 GeV, 10% below 0.1 GeV and 20% above 10 GeV. We therefore propagate these  
 223 uncertainties using modified effective areas bracketing the nominal ones (P6\_v3\_diffuse).

224 For this fit over the range 0.1 – 100 GeV we obtained an integral photon flux of  $(4.14 \pm 0.02$   
 225  $\pm 0.32) \times 10^{-6} \text{cm}^{-2} \text{s}^{-1}$  and a corresponding energy flux of  $(4.11 \pm 0.02 \pm 0.27) \times 10^{-9}$   
 226  $\text{erg cm}^{-2} \text{s}^{-1}$ .

227 We studied alternative spectral shapes beginning with the cut-off function  $\exp[-(E/E_0)^b]$ .  
 228 The 46 gamma-ray pulsars discussed in Abdo et al. (2010a) are generally well-described by a  
 229 simple exponential cutoff,  $b = 1$ , a shape predicted by outer magnetosphere emission models  
 230 (see the Discussion, below). Models where gamma-ray emission occurs closer to the neutron  
 231 star can have sharper “super-exponential” cutoffs, e.g.  $b = 2$ . Leaving free the exponential  
 232 index  $b$  we obtained  $N_0 = (1.59 \pm 0.13 \pm 0.09) \times 10^{-9} \text{cm}^{-2} \text{s}^{-1} \text{GeV}^{-1}$ ,  $\Gamma = (1.18 \pm 0.03$   
 233  $\pm 0.04)$ ,  $E_0 = 1.58 \pm 0.19 \pm 0.11 \text{GeV}$  and  $b = (0.81 \pm 0.03 \pm 0.06)$ . As previously reported  
 234 for the analysis of Vela pulsar (Abdo et al. 2010b),  $b < 1$  can be interpreted by a blend of  $b$   
 235  $= 1$  spectra with different cutoff energies. Figure 6 shows the results of the phase-averaged  
 236 spectrum in case of  $b$  free (dashed line) and  $b$  fixed to 1 (solid line). Using the likelihood  
 237 ratio test we found that the hypothesis of  $b=2$  can be excluded since the likelihood of this fit  
 238 being a good representation of the data is much greater than for a power-law fit (logarithm  
 239 of the likelihood ratio being 396). We have also tried different spectral shapes, like a broken  
 240 power law, but the fit quality does not improve (the logarithm of the likelihood ratio is 212).

241

### 242 4.3. Phase-resolved analysis

243 We divided the pulse profile in variable-width phase bins, each one containing 2000  
 244 photons according to the energy-dependent cut defined in Section 4.1. This choice of bin-  
 245 ning provides a reasonable compromise between the number of photons needed to perform

246 a spectral fit and the length of the phase intervals, that should be short enough to sample  
 247 fine details on the lightcurve, while remaining comfortably larger than the rms of the timing  
 248 solution (Sec. 3). We have performed a maximum likelihood spectral analysis, similar to  
 249 the phase-averaged one, in each phase bin assuming a power law with exponential cut-off  
 250 describing the spectral shape. Using the likelihood ratio test we checked that we can reject  
 251 the power law at a significance level greater than 5 sigma in each phase interval. Following  
 252 the results on phase-averaged analysis of Geminga, we have modeled the spectrum in each  
 253 phase interval with a power law with exponential cutoff. Such a model yields a robust fit  
 254 with a logarithm of the likelihood ratio greater than 430 in each phase interval. Figure 7  
 255 (below) shows the evolution of the spectral parameters across Geminga’s rotational phase.  
 256 In particular, the energy cutoff trend provides a good estimate of the high energy emission  
 257 variation as a function of the pulsar phase. Table 3 summarizes the results of the spectral  
 258 fit in each phase bin. In this case we have fixed all the spectral parameters of all the nearby  
 259  $\gamma$ -ray sources and of the two diffuse backgrounds to the values obtained in the phase aver-  
 260 aged analysis, rescaled for the phase bin width.

261 To obtain *Fermi*-LAT spectral points we divided our sample into logarithmically-spaced  
 262 energy bins (4 bins per decade starting from 100 MeV) and then applied the maximum like-  
 263 lihood method in each bin. For each energy bin we have used a model with all the nearby  
 264 sources as well as Geminga described by power law with fixed spectral index. We have con-  
 265 sidered only energy bins in which the source significance was greater than  $3\sigma$ . From the fit  
 266 results we then evaluated the integral flux in each energy bin. This method does not take  
 267 energy dispersion into account and correlations among the energy bins. To obtain the points  
 268 of the Spectral Energy Distributions (SEDs) we multiplied each bin by the mean energy  
 269 value of the bin taking into account the spectral function obtained by the overall fit. Figures  
 270 9 to 12 in the Appendix show the SEDs obtained in each phase interval. The fluxes in Y-axis  
 271 are not normalized to the phase bin width, whereas in Table 3 of the Appendix the fluxes  
 272 are normalized. Figure 7 shows the phase evolution of the spectral index and cut-off energy,  
 273 respectively. The spectral index reaches a local minimum around P1 ( $\phi \sim 0.14 - 0.15$ ) and,  
 274 after a sudden increase, begins to decrease again in the “first interpeak” region, reaching a  
 275 minimum of  $\Gamma \sim 1.1$  around the leading edge of P2 ( $\phi \sim 0.60 - 0.61$ ). It then starts to rise  
 276 again in the phase interval from P2 to the “second interpeak” region ( $\phi = 0.9 - 1.0$ ).

277 The cut-off energy evolves quite differently as a function of the rotational phase. It closely fol-  
 278 lows the pulse profile, thus confirming the observations performed by EGRET (Fierro et al.  
 279 1998), which unveiled a correlation between hardness ratio and pulse profile. As shown in  
 280 EGRET data and recently confirmed by AGILE (Pellizzoni et al. 2009), the hardest compo-  
 281 nent is P2: our phase-resolved scan points to a cut-off around 3 GeV and a spectral index of  
 282  $\sim 1.0$  that become softer through the peak. P1 appears to be softer, with a cut-off energy  
 283 slightly greater than 2 GeV and a spectral index  $\Gamma \sim 1.2$ .

284 The phase-resolved spectra show that Geminga’s emission in the bridge (or “first interpeak”)  
 285 phase interval ( $\phi = 0.2 - 0.52$ ) is quite different from the Crab (Abdo et al. 2010c) or Vela  
 286 pulsars (Fierro et al. 1998; Abdo et al. 2009a). For the Crab pulsar the bridge emission  
 287 shows no evolution and drops to an intensity level comparable to the off pulse emission,  
 288 while for the Vela pulsar it varies substantially but is always seen at high energies. The  
 289 “first interpeak” of Geminga, instead, becomes harder and remains quite strong at high en-  
 290 ergies, as can be also seen in Figure 3. Another difference with respect to the Vela pulsar is  
 291 that Geminga does not have a third peak like the one observed at GeV energies in the Vela  
 292 pulsar (Abdo et al. 2009a).

293 The analysis of the “second interpeak” region around  $\phi = 0.9 - 1.0$  shows significant emission  
 294 up to  $\sim 2$  GeV (Figure 3). Moreover the spectrum in this phase interval has been fit with  
 295 a power law with exponential cut-off, obtaining a spectral index  $\Gamma = (1.48 \pm 0.17)$  and  $E_0$   
 296  $= (0.87 \pm 0.19)$  GeV, with systematic uncertainties in agreement with those evaluated in  
 297 the phase averaged analysis. A pure power law fit can be rejected with a  $\sim 8\sigma$  confidence  
 298 level, thus confirming the presence of the cut-off. The presence of the “second interpeak”  
 299 component is also visible in the maps of Figure 8, where the emission in this phase region is  
 300 not visible at high energies, as expected owing to the spectral cut-off.

301 Analyzing the phase evolution of the spectral parameters in Figure 7 it seems that no abrupt  
 302 changes occur in this phase interval and that this emission may be related to the wings of  
 303 the peaks. This fact, together with the newly detected off-peak emission, favors a pulsar  
 304 origin of such “second interpeak” emission, rather than an origin in a surrounding region.  
 305 The detection of off-peak emission, rendered possible by the outstanding *Fermi* statistics,  
 306 is a novelty of Geminga’s high energy behaviour.

## 307 5. Discussion

### 308 5.1. Light curves and beam geometry

309 The unprecedented photon statistics collected by *Fermi* LAT allows for tighter observa-  
 310 tional constraints on emission models. The absence of radio emission characterizing Geminga  
 311 clearly favors models where the high energy emission occurs in the outer magnetosphere of  
 312 the pulsar.

313 Polar Cap (PC) models, where high energy emission is located near the neutron star surface  
 314 (Daugherty and Harding 1996), are unlikely to explain the Geminga pulsar, since the line  
 315 of sight is necessarily close to the magnetic axis for such models where one expects to see  
 316 radio emission.

317 The current evidence against low-altitude emission in  $\gamma$ -ray pulsars (Abdo et al. 2009l) can

318 also be supplemented by constraints on a separate physical origin. In PC models,  $\gamma$  rays  
 319 created near the neutron star surface interact with the high magnetic fields of the pulsar,  
 320 producing sharp cut-offs in the few to  $\sim 10$  GeV energy regime. Moreover, the maximum  
 321 observed energy of the pulsed photons observed must lie below the  $\gamma$ -B pair production  
 322 mechanism threshold, providing a lower bound to the altitude of the  $\gamma$ -ray emission. Ac-  
 323 cording to Baring (2004), the lower limit for the altitude of the production region  $r$  could  
 324 be estimated taking advantage of the maximum energy detected for pulsed photons  $\epsilon_{max}$  as  
 325  $r \geq (\epsilon_{max} B_{12} / 1.76 \text{ GeV})^{\frac{2}{7}} P^{-\frac{1}{7}} R_*$  where  $P$  is the spin period,  $R_*$  is the stellar radius and  $B_{12}$   
 326 is the surface magnetic field in units of  $10^{12} G$ . For pulsed photons of  $\epsilon_{max} \sim 18$  GeV, we  
 327 obtain  $r_{min} \geq 2.7 R_*$ , a value clearly precluding emission very near the stellar surface, adding  
 328 to the advocacy for a slot gap or outer gap acceleration locale for the emission in this pulsar.  
 329 Outer Gap (OG) models (Cheng et al. 1986; Romani 1996; Zhang & Cheng 2001), where  
 330 the high energy emission extends between the null charge surface and the light cylinder,  
 331 the two-pole caustic (TPC) models (Dyks and Rudak 2003) associated with slot gap (SG)  
 332 (Muslimov and Harding 2004), where the emission is located along the last open field lines  
 333 between the neutron star surface and the light cylinder, or a striped wind model (Pétri  
 334 2009), where the emission originates outside the light cylinder, could produce the observed  
 335 light curve and spectrum. Nevertheless, the observed peak separation of 0.5 is unlikely for a  
 336 middle aged pulsar like Geminga in the OG model, if it is true that emission moves to field  
 337 lines closer to the magnetic axis as pulsars age. For the OG model this drift leads to  $< 0.5$   
 338 peak separations. For TPC models 0.5 peak separation can occur in spite of this shift, that  
 339 is, for all ages and spin-down luminosities.  
 340 Following the Atlas of  $\gamma$ -ray light curves compiled by Watters et al. (2009), we can use  
 341 Geminga’s light curve to estimate, for each model, the star’s emission parameters, namely  
 342 the Earth viewing angle  $\zeta_E$  with respect to the neutron star spin axis, and the inclination  
 angle  $\alpha$  between the star’s magnetic and rotation axes. Table 2 summarizes the observed

Model	$\alpha$	$\zeta_E$	$f_\Omega$
TPC	30 – 80, 90	90, 55 – 80	0.7 – 0.9, 0.6 – 0.8
OG	10 – 25	85	0.1 – 0.15

Table 2: Earth viewing angles  $\zeta_E$ , inclination angles  $\alpha$  and beaming factor  $f_\Omega$  for Geminga, as predicted by Watters et al. (2009) for Outer Gap (OG) and Two Pole Caustics (TPC) models.

343 parameters and gives the estimated beaming correction factor  $f_\Omega(\alpha, \zeta_E)$ , which is model-  
 344 sensitive. It is given by (Watters et al. 2009):  
 345

$$f_\Omega(\alpha, \zeta_E) = \frac{\int F_\gamma(\alpha; \zeta, \phi) \sin(\zeta) d\zeta d\phi}{2 \int F_\gamma(\alpha; \zeta_E, \phi) d\phi} \quad (2)$$

346 where  $F_\gamma(\alpha; \zeta, \phi)$  is the radiated flux as a function of the viewing angle  $\zeta$  and the pulsar  
 347 phase  $\phi$ . In this equation, the numerator is the total emission over the full sky, and the  
 348 denominator is the expected phase-averaged flux for the light curve seen from Earth.  
 349 The total luminosity radiated by the pulsar is then given by  $L_\gamma = 4\pi f_\Omega F_{obs} D^2$  where  $F_{obs}$   
 350 is the observed phase-averaged energy flux over 100 MeV and  $D = 250_{+120}^{-62}$  pc is the pulsar  
 351 distance (Faherty et al. 2007). The estimated averaged luminosity is then  $L_\gamma = 3.1 \times 10^{34} f_\Omega$   
 352  $\text{erg s}^{-1}$ , yielding a  $\gamma$ -ray efficiency  $\eta_\gamma = \frac{L_\gamma}{\dot{E}} = 0.15 f_\Omega (d/100\text{pc})^2$ .  
 353 Ideally, geometrical values in Table 2 should be compared with independent estimates, com-  
 354 ing e.g. for radio polarization or from the geometry of the pulsar wind nebula (Ng & Romani  
 355 2004, 2008).  
 356 Owing to the lack of radio emission, the only geometrical constraints available for Geminga  
 357 come from the X-ray observations which have unveiled a faint bow shock structure, due to  
 358 the pulsar motion in the interstellar medium (Caraveo et al. 2003) and a inner tail struc-  
 359 ture (De Luca et al. 2006; Pavlov et al. 2006), while phase resolved spectroscopy yielded a  
 360 glimpse of the geometry of the emitting regions as the neutron star rotates (Caraveo et al.  
 361 2004).  
 362 The shape of the bow shock feature constrains its inclination to be less than  $30^\circ$  with respect  
 363 to the plane of the sky. Since such a feature is driven by the neutron star proper motion,  
 364 the constraint applies also to the pulsar proper motion vector and thus, presumably, to its  
 365 rotation axis, as is the case for the Vela Pulsar (Caraveo et al. 2001), pointing to an earth  
 366 viewing angle ranging from 60 to 90 degrees.  
 367 Analysing the pulsar spectral components along its rotational phase, Caraveo et al. (2004)  
 368 concluded that the observed behaviour could be explained in the frame of an almost aligned  
 369 rotator seen at high inclination.  
 370 However rough, such constraints would definitely favour the OG model pointing to a beam-  
 371 ing factor of 0.1-0.15. Such a value turns out to be in agreement also with the heuristic  
 372 luminosity law  $\eta \simeq \left(\dot{E}/10^{33}\right)^{-0.5}$  given by Arons (1996) and Watters et al. (2009), that for  
 373 the Geminga parameters should yield a value of  $\sim 17\%$ . For the nominal parallax distance  
 374 of 250 pc, a beaming factor of 0.15 would yield a luminosity of  $L_\gamma = 4.6 \times 10^{33} \text{ erg s}^{-1}$ .  
 375 We note that TPC models, characterized by higher efficiency, would yield higher luminosity  
 376 which would account for the entire rotational energy loss for a distance of  $\sim 300$  pc, well  
 377 within the distance uncertainty. On the other hand, a 100% efficiency would translate into a  
 378 distance of 730 pc for the OG model, providing a firm limit on the maximum source distance.



## 5.2. Phase resolved spectroscopy

379

380 The power law with exponential cut-off describes only approximately the phase-averaged  
 381 spectrum of Geminga, since several spectral components contribute at different rotational  
 382 phases. The phase-resolved analysis that we have performed is thus a powerful tool for  
 383 probing the emission of the Geminga pulsar.

384 Figure 7 shows a sudden change in the spectral index around each peak maximum. The  
 385 spectrum appears to be very hard in the “first interpeak” region between P1 and P2, with  
 386 an index close to  $\Gamma \sim 1.1$  and softens quickly after the peak maximum and in the “second  
 387 interpeak” to  $\Gamma \sim 1.5$ . Caustic models such as OG and TPC predict such behavior as a  
 388 result of the change in emission altitude with energy. Sudden changes in the energy cut-off  
 389 are also predicted, as is also seen for Geminga. Large variations in the spectral index and  
 390 energy cut-off as a function of the pulsar phase have already been seen in other pulsars, such  
 391 as the Crab pulsar (Abdo et al. 2010c) or PSR J2021+3651 (Abdo et al. 2009e).

392 The persistence of an energy cut-off in the “second interpeak” region suggests pulsar emission  
 393 extending over the whole rotation, further supporting the TPC model for Geminga. A similar  
 394 “second interpeak” has been also observed by Fermi-LAT in PSR J1836+5925, known as the  
 395 “next Geminga” (Halpern et al. 2007). Although Geminga is significantly younger, the two  
 396 pulsars share other interesting features, including very similar spectral indexes and  
 397 energy cut-offs in the phase-averaged spectrum, and comparable X-ray spectra (Abdo et al.  
 398 2010d).

399

## 6. Conclusions

400 In this Paper we presented the analysis of Geminga based on data collected during the  
 401 first year of *Fermi* operations. The large collecting area of the LAT allows a timing solution  
 402 to be obtained solely from  $\gamma$ -ray data.

403 The study of the light curve showed the evolution of the pulse profile with energy, unveiling  
 404 the shrinking of the peaks with increasing energy and providing insights on the highest  
 405 energies with unprecedented detail. Although the phase-averaged spectrum is consistent  
 406 with a power law with exponential cut-off, the phase-resolved analysis showed a much richer  
 407 picture of different spectral components intervening at different rotational phases. The  
 408 phase-resolved analysis has also allowed the detection of the “second interpeak” emission  
 409 indicating a pulsar emission extending over all phases. This feature, never seen before in  
 410 Geminga, was recently also seen by *Fermi* LAT in PSR J1836+5925 (Abdo et al. 2010d).

411 Our results favor the outer magnetospheric origin for the  $\gamma$ -ray emission. The distance  
 412 uncertainty allows for reasonable values of efficiency for both OG and TPC models, although

413 the efficiency for the TPC model becomes too large for distance values just above the nom-  
 414 inal one. Future improvements in estimating the distance of Geminga will help to better  
 415 strengthen the conclusions and constraining outer magnetospheric models.  
 416 The light curve and phase-resolved spectral studies provide a much stronger constraint on  
 417 the model geometry. The inclination and viewing angle phase space for peak separation of  
 418 0.5 is very small for the OG, which however provides values compatible with those obtained  
 419 from the analysis of Geminga’s X-ray behaviour. On the other hand, TPC geometry would  
 420 seem more natural for pulsars of Geminga’s age that have large gaps. Pulsed emission at all  
 421 phases is a common feature of the TPC geometry. It occurs infrequently for OG geometries,  
 422 although is present for the large  $\zeta_E$  solutions invoked here for Geminga.

423 The *Fermi* LAT Collaboration acknowledges generous ongoing support from a number  
 424 of agencies and institutes that have supported both the development and the operation of the  
 425 LAT as well as scientific data analysis. These include the National Aeronautics and Space  
 426 Administration and the Department of Energy in the United States, the Commissariat à  
 427 l’Energie Atomique and the Centre National de la Recherche Scientifique / Institut National  
 428 de Physique Nucléaire et de Physique des Particules in France, the Agenzia Spaziale Italiana  
 429 and the Istituto Nazionale di Fisica Nucleare in Italy, the Ministry of Education, Culture,  
 430 Sports, Science and Technology (MEXT), High Energy Accelerator Research Organization  
 431 (KEK) and Japan Aerospace Exploration Agency (JAXA) in Japan, and the K. A. Wallen-  
 432 berg Foundation, the Swedish Research Council and the Swedish National Space Board in  
 433 Sweden. Additional support for science analysis during the operations phase is gratefully  
 434 acknowledged from the Istituto Nazionale di Astrofisica in Italy and the Centre National  
 435 d’Études Spatiales in France.

## 436 **Appendix A: detailed results from phase-resolved spectral analysis**

437 In this Appendix we report all the numerical results and the spectral Energy Distribu-  
 438 tions (SEDs) obtained from the phase-resolved spectral analysis of Geminga. Table 3 shows  
 439 the spectral parameters obtained from the spectral fit in each phase interval, while Figures  
 440 from 9 to 12 show the plots of all the SEDs.

## 441 **REFERENCES**

442 Abdo, A. A., et al. 2009a, ApJ, 696, 1084

- 443 Abdo, A. A., et al. 2009b, *ApJ*, 695, L72
- 444 Abdo, A. A., et al. 2009c, *ApJ*, 699, L102
- 445 Abdo, A. A., et al. 2009d, *ApJ*, 699, 1171
- 446 Abdo, A. A., et al. 2009e, *ApJ*, 700, 1059
- 447 Abdo, A. A., et al. 2009f, *Science*, 325, 848
- 448 Abdo, A. A., et al. 2009g, *Science*, 325, 840
- 449 Abdo, A. A., et al. 2009h, *Astroparticle Phys.*, 32, 193.
- 450 Abdo, A. A., et al. 2009l, *ApJS*, 183, 46
- 451 Abdo, A. A., et al. 2010a, *ApJS*, 187, 460.
- 452 Abdo, A. A., et al. 2010b, *ApJ*, 713, 154
- 453 Abdo, A. A., et al. 2010c, *ApJ*, 708, 1254
- 454 Abdo, A. A., et al. 2010d, *ApJ*, 712, 1209
- 455 Arons, J., 1996, *A&AS*, 120, C49
- 456 Atwood, W. B., et al. 2009, *ApJ*, 697, 1071
- 457 Baring, M. G. 2004, *AdSpR*, 33, 552
- 458 Bennett, K., et al. 1977, *A&A*, 56, 469
- 459 Bertsch, D. L., et al. 1992, *Nature*, 357, 306
- 460 Bignami, G. F., Caraveo, P. A., & Lamb, R. C. 1983, *ApJ*, 272, L9
- 461 Bignami, G. F., Caraveo, P. A., Paul, J. A., Salotti, L., & Vigroux, L. 1987, *ApJ*, 319, 358
- 462 Bignami, G. F., Caraveo, P. A., & Paul, J. A. 1988, *A&A*, 202, L1
- 463 Bignami, G. F., & Caraveo, P. A. 1992, *Nature*, 357, 287
- 464 Bignami, G. F., Caraveo, P. A., & Mereghetti, S. 1993, *Nature*, 361, 704
- 465 Bignami, G. F., & Caraveo, P. A. 1996, *ARA&A*, 34, 331
- 466 Caraveo, P. A., Bignami, G. F., Mignani, R., & Taff, L. G. 1996, *ApJ*, 461, L91

- 467 Caraveo, P. A., Lattanzi, M. G., Massone, G., Mignani, R. P., Makarov, V. V., Perryman,  
468 M. A. C., & Bignami, G. F. 1998, *A&A*, 329, L1
- 469 Caraveo, P. A., DeLuca, A., Mignani, R., Bignami, G. F. 2001, *ApJ*, 561, 930
- 470 Caraveo, P. A., Bignami, G. F., DeLuca, A., Mereghetti, S., Pellizzoni, A., Mignani, R., Tur,  
471 A., & Becker, W. 2003, *Science*, 301, 1345
- 472 Caraveo, P. A., De Luca, A., Mereghetti, S., Pellizzoni, A., & Bignami, G. F. 2004, *Science*,  
473 305, 376
- 474 Casandjian, J.-M. & Grenier, I. A. 2008, *A&A*, 489, 849
- 475 Cheng, K. S., Ho, C., Ruderman, M. 1986, *ApJ*, 300, 500
- 476 Daugherty, J. K. and Harding, A. K., 1996, *ApJ*, 458, 278
- 477 De Luca, A., Caraveo, P. A., Mereghetti, S., Negroni, M., & Bignami, G. F. 2005, *ApJ*, 623,  
478 1051
- 479 de Luca, A., Caraveo, P. A., Mattana, F., Pellizzoni, A., & Bignami, G. F. 2006, *A&A*, 445,  
480 L9
- 481 Dyks, J. and Rudak, B., 2003, *ApJ*, 598, 1201
- 482 Faherty, J., Walter, F. M., & Anderson, J. 2007, *Ap&SS*, 308, 225
- 483 Fichtel, C. E., et al. 1975, *ApJ*, 198, 163
- 484 Fierro, J. M., Michelson, P. F., Nolan, P. L., & Thompson, D. J. 1998, *ApJ*, 494, 734
- 485 Halpern, J. P., & Tytler, D. 1988, *ApJ*, 330, 201
- 486 Halpern, J. P., & Holt, S. S. 1992, *Nature*, 357, 222
- 487 Halpern, J. P., Camilo, F., & Gotthelf, E. V. 2007, *ApJ*, 668, 1154
- 488 Hobbs, G. B., Edwards, R. T., & Manchester, R. N. 2006, *MNRAS*, 369, 655
- 489 Jackson, M. S., & Halpern, J. P. 2005, *ApJ*, 633, 1114
- 490 Kniffen, D. A., et al. 1975, *Proc. 14th Internat. Cosmic Ray Conf.* , 1, 100
- 491 Masnou, J. L., et al. 1981, *Proc. 17th Internat. Cosmic Ray Conf.* , 1, 177

- 492 Mattox, J. R., Bertsch, D. L., Fichtel, C. E., Hartman, R. C., Kniffen, D. A., & Thompson,  
493 D. J. 1992, *ApJ*, 401, L23
- 494 Mattox, J. R., Halpern, J. P., & Caraveo, P. A. 1998, *ApJ*, 493, 891
- 495 Mayer-Hasselwander, H. A., et al. 1994, *ApJ*, 421, 276
- 496 Muslimov, A. G. and Harding, A. K., *ApJ*, 588, 430
- 497 Ng, C.-Y. & Romani, R. W. 2004, *ApJ*, 601, 479
- 498 Ng, C.-Y. & Romani, R. W. 2008, *ApJ*, 673, 411
- 499 Pavlov, G. G., Sanwal, D., & Zavlin, V. E. 2006, *ApJ*, 643, 1146
- 500 Pellizzoni, A., et al. 2009, *ApJ*, 691, 1618
- 501 Pétri, J. 2009, *A&A*, 503, 13
- 502 Romani, R. W., 1996, *ApJ*, 470, 469
- 503 Smith, D. A., et al. 2008, *A&A*, 492, 923
- 504 Standish, E. M., JPL Planetary and Lunar Ephemerides, DE405/LE405, Memo IOM 312.F-  
505 98-048 (1998)
- 506 Strong, A. W., Moskalenko, I. V., & Reimer, O. 2004, *ApJ*, 613, 962
- 507 Strong, A. W., Moskalenko, I. V., Reimer, O., Digel, S., & Diehl, R. 2004, *A&A*, 422, L47
- 508 Swanenburg, B. N., et al. 1981, *ApJ*, 243, L69
- 509 Tavani, M., et al. 2009, *A&A*, 502, 995
- 510 Thompson, D. J. 2004, in *Astroph. and Space Sci.* 304, *Cosmic Gamma-Ray Sources*, ed. K.  
511 S. Cheng & G. E. Romero (Kluwer: Dordrecht), 149
- 512 Watters, K. P. and Romani, R. W. and Weltevrede, P. and Johnston, S., 2009, *ApJ*, 695,  
513 1289
- 514 Zhang, L., & Cheng, K. S. 2001, *MNRAS*, 320, 477

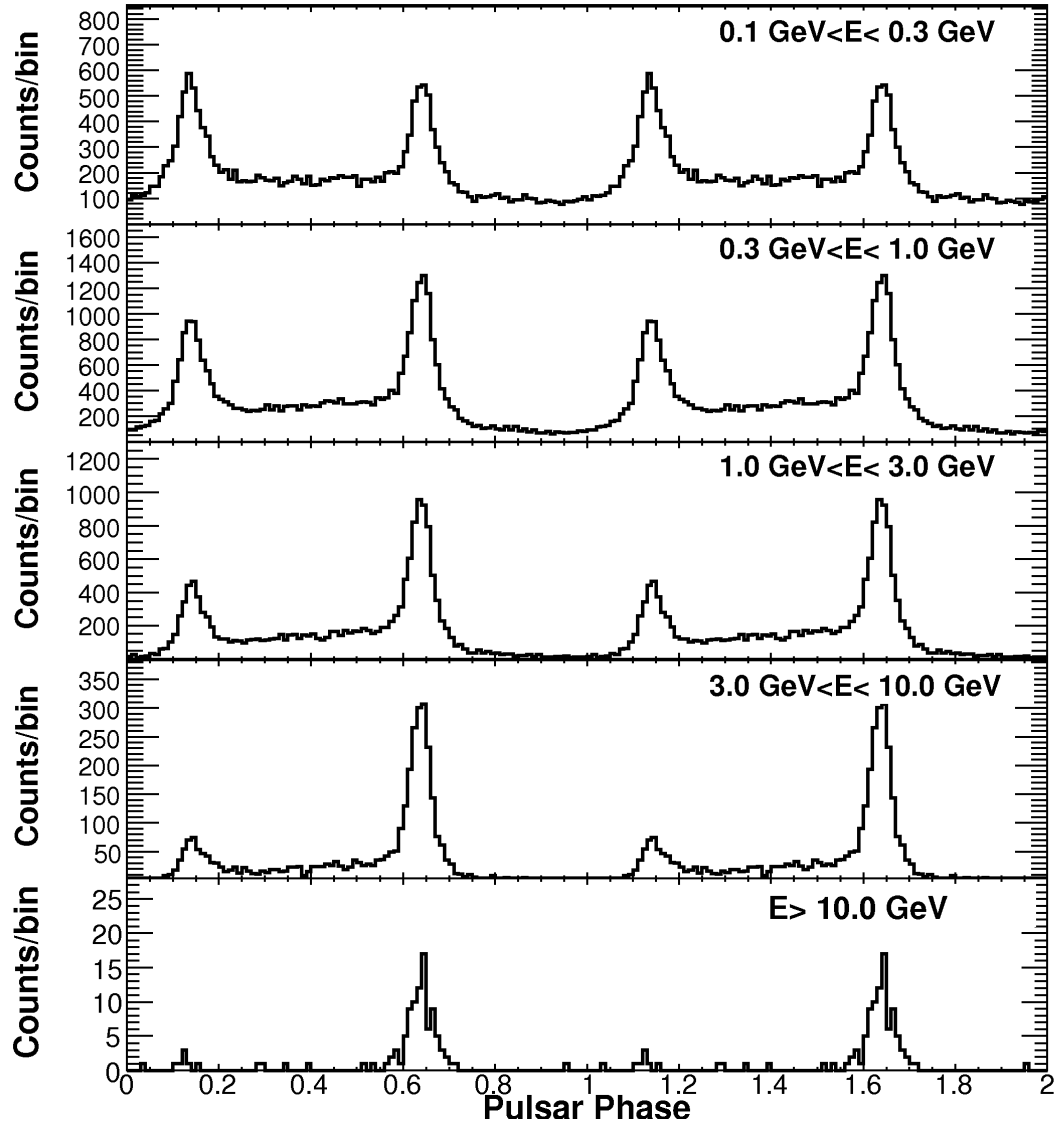


Fig. 3.— Geminga light curves in five energy ranges (0.1–0.3 GeV, 0.3–1 GeV, 1–3 GeV, 3–10 GeV, > 10 GeV). Each light curve is shown over two pulse periods and contains 100 bins/period.

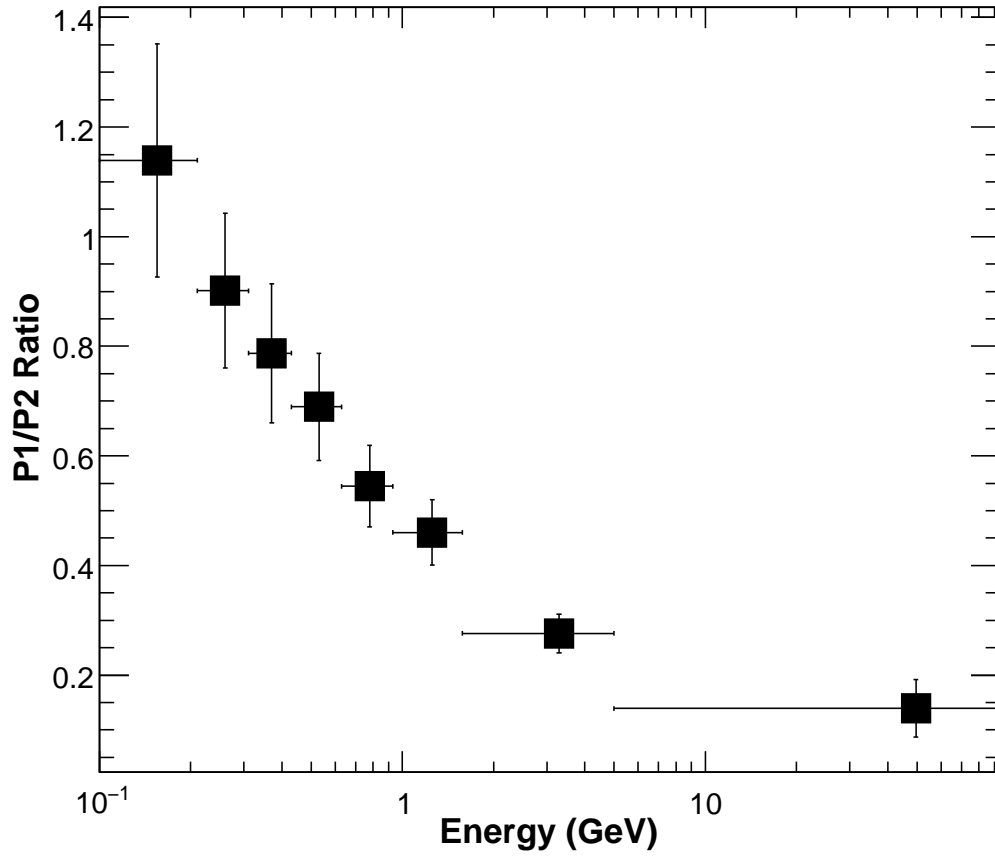


Fig. 4.— Evolution of the ratio P1/P2 with energy, plotted in variable-width energy bins, each one containing 10000 events.

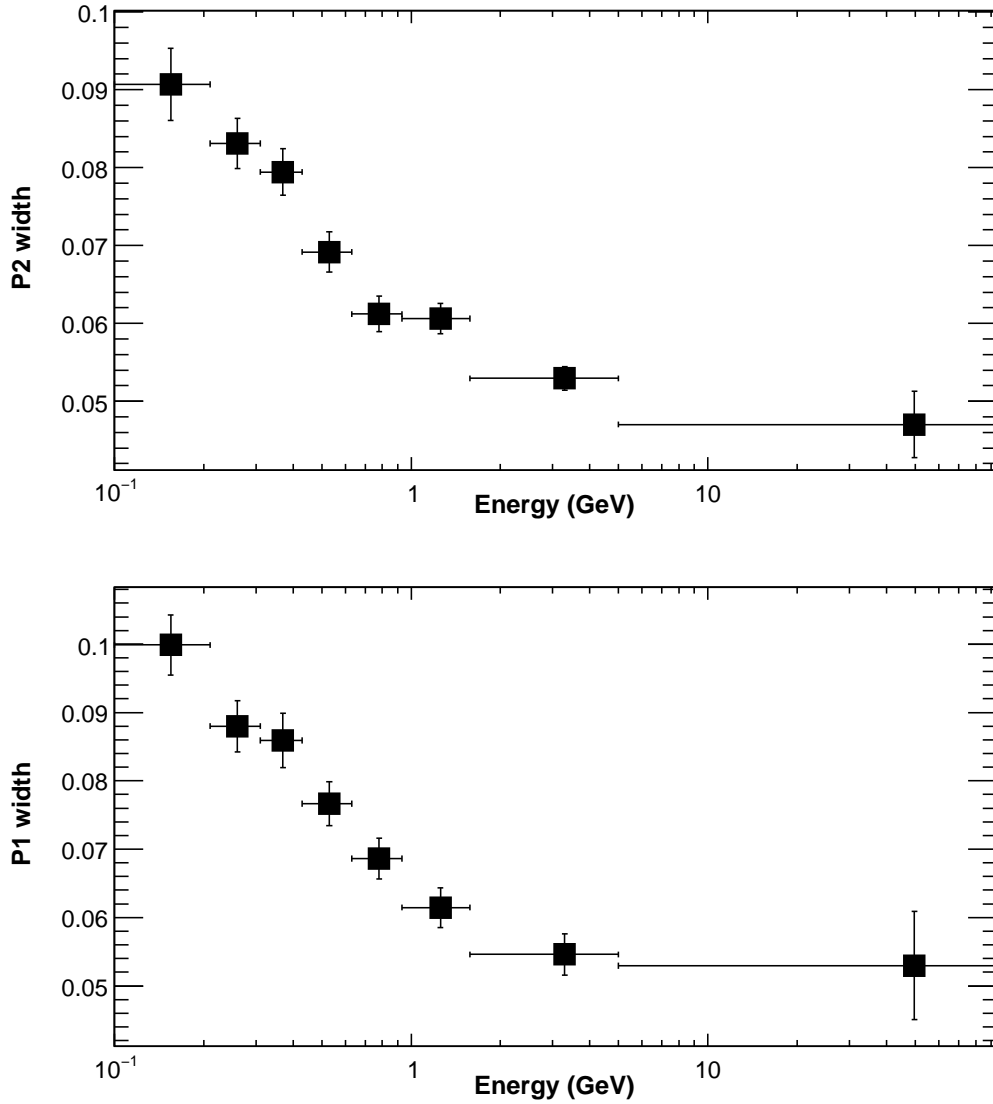


Fig. 5.— Evolution with energy of the FWHM of P1 (*bottom*) and P2 (*top*), plotted in variable-width energy bins, each one containing 10,000 events. Both peaks narrow at increasing energies.



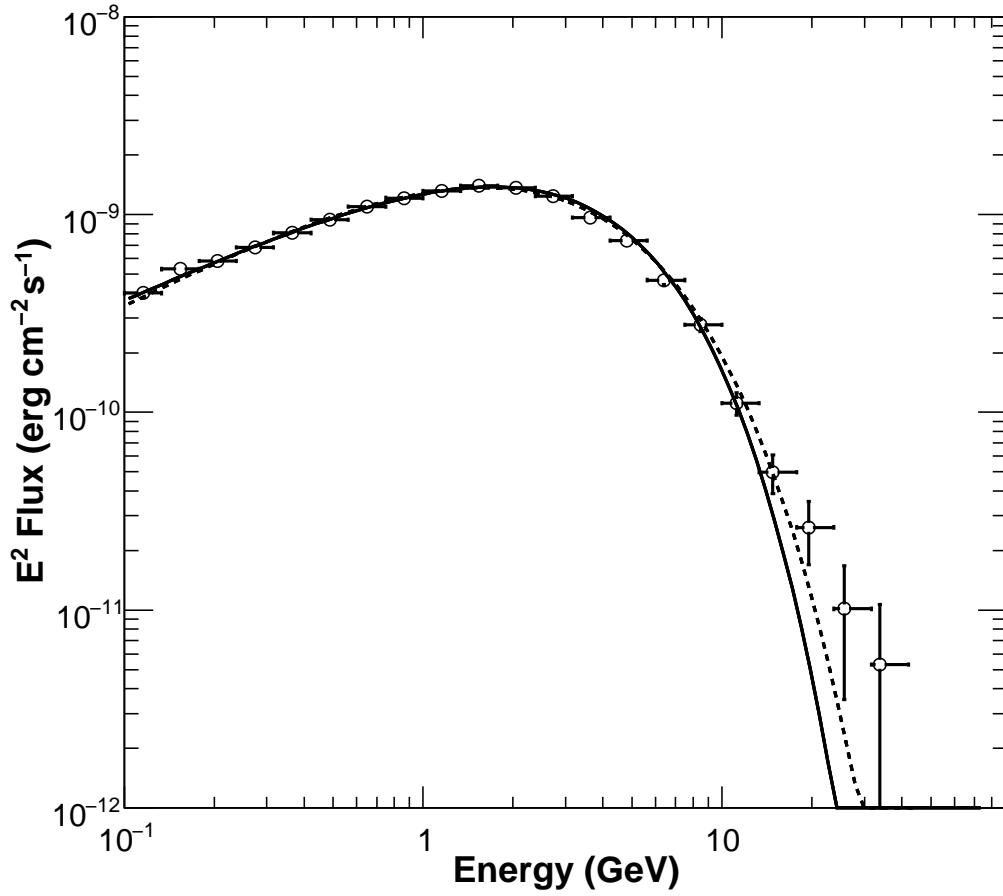


Fig. 6.— Phase-averaged Spectral Energy Distribution (SED) of the Geminga pulsar. The solid line represents the best fit power law with exponential cutoff (i.e  $b=1$ ), while the dashed one represents the best fit power law with exponential cutoff with free exponential index (in this case the result is  $b=0.81$ ). The LAT spectral points (open circles) are obtained using the maximum likelihood method described in Section 4.2

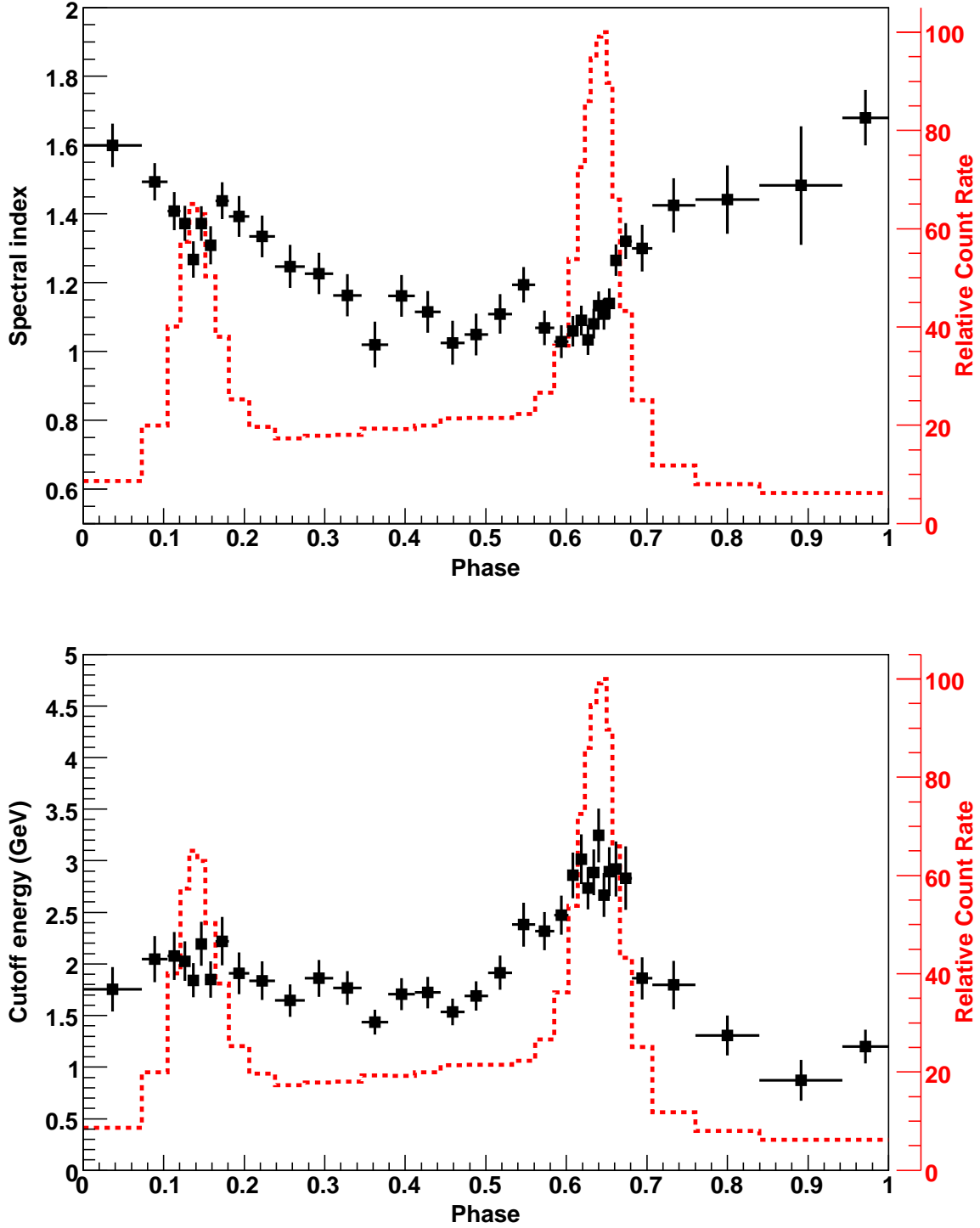


Fig. 7.— Phase evolution of the spectral index (*top*) and energy cut-off (*bottom*) above 0.1 GeV as the function of the pulse phase, divided in phase bins each containing 2000 photons. Vertical bars indicate the combined statistical and systematic uncertainties. For each phase interval (defined in Table 3 in the Appendix) a power law with exponential cut-off has been assumed. The dashed histogram represents the *Fermi*-LAT light curve above 0.1 GeV in variable-width phase bins of 2000 photons/bin.

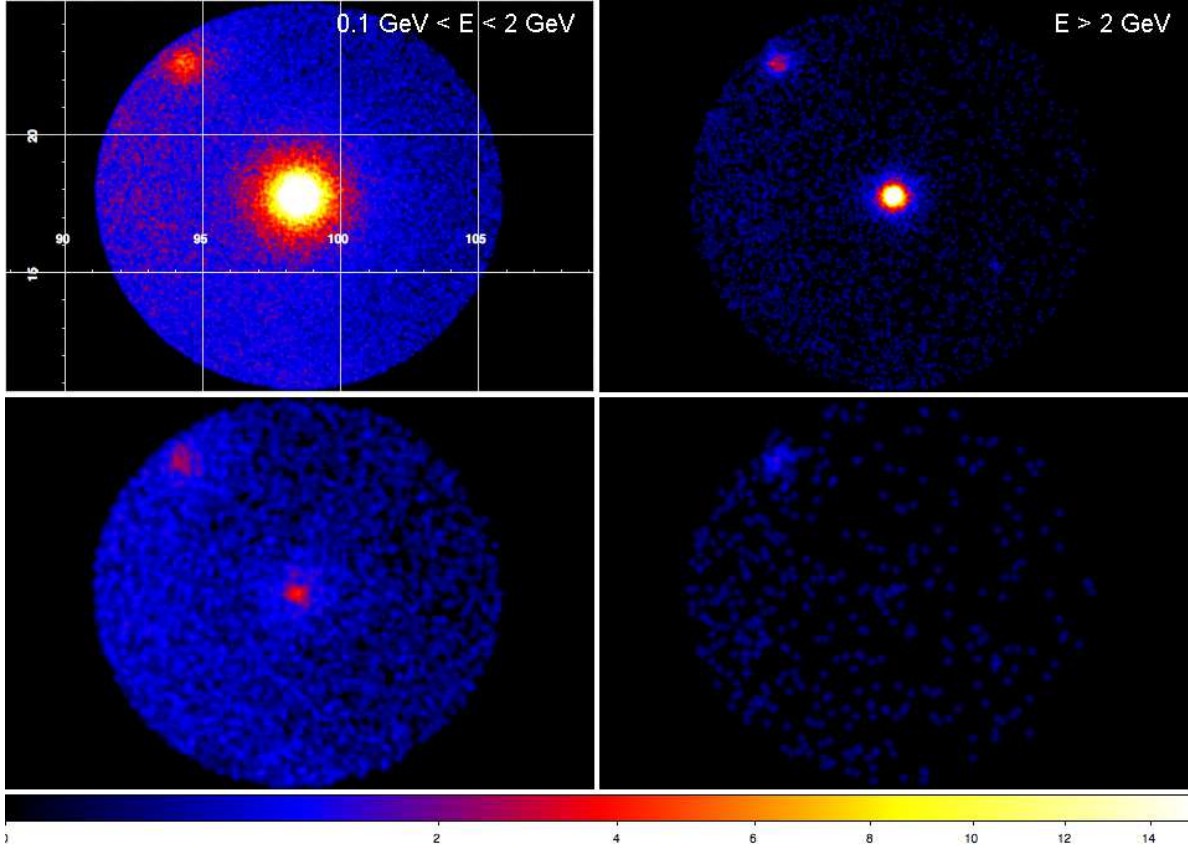


Fig. 8.— Maps representing the phase interval ( $\phi=0.0 - 0.9$ , *top row*) compared to the second interpeak ( $\phi=0.9-1.0$ , *bottom row*), in the 2 energy bands  $0.1-2 \text{ GeV}$  and  $> 2 \text{ GeV}$ . Each map represents the photons within  $7^\circ$  from Geminga, binned in pixels of  $0.045^\circ$  (*top row*) and  $0.09^\circ$  (*bottom row*), smoothed with a gaussian filter with a radius of 2 pixels. In the upper left panel we reported the Right Ascension in horizontal axis and the Declination in the vertical axis. Bottom row shows that the offpeak point source image is visible at low energies but vanishes at  $E > 2 \text{ GeV}$  due to the spectral cut-off.

$\phi_{min}$	$\phi_{max}$	Flux $> 0.1$ GeV ( $\times 10^{-7} \text{ cm}^{-2} \text{ s}^{-1}$ )	Spectral index	Cut-off energy (GeV)
0.000	0.073	$1.72 \pm 0.07$	$1.67 \pm 0.08$	$1.19 \pm 0.16$
0.073	0.104	$4.49 \pm 0.15$	$1.59 \pm 0.06$	$1.75 \pm 0.21$
0.104	0.120	$9.14 \pm 0.27$	$1.49 \pm 0.05$	$2.04 \pm 0.22$
0.120	0.131	$12.46 \pm 0.36$	$1.40 \pm 0.05$	$2.07 \pm 0.23$
0.131	0.141	$14.24 \pm 0.40$	$1.37 \pm 0.05$	$2.02 \pm 0.19$
0.141	0.151	$13.09 \pm 0.37$	$1.26 \pm 0.05$	$1.84 \pm 0.16$
0.151	0.164	$10.74 \pm 0.31$	$1.37 \pm 0.05$	$2.19 \pm 0.21$
0.164	0.181	$7.76 \pm 0.23$	$1.30 \pm 0.05$	$1.85 \pm 0.17$
0.181	0.206	$5.35 \pm 0.17$	$1.43 \pm 0.05$	$2.21 \pm 0.23$
0.206	0.238	$3.89 \pm 0.13$	$1.39 \pm 0.05$	$1.91 \pm 0.20$
0.238	0.275	$3.30 \pm 0.11$	$1.33 \pm 0.06$	$1.83 \pm 0.18$
0.275	0.310	$3.36 \pm 0.11$	$1.24 \pm 0.06$	$1.64 \pm 0.15$
0.310	0.345	$3.29 \pm 0.11$	$1.22 \pm 0.05$	$1.86 \pm 0.17$
0.345	0.378	$3.36 \pm 0.11$	$1.16 \pm 0.06$	$1.76 \pm 0.16$
0.378	0.411	$3.24 \pm 0.11$	$1.02 \pm 0.06$	$1.43 \pm 0.12$
0.411	0.443	$3.51 \pm 0.11$	$1.16 \pm 0.06$	$1.70 \pm 0.15$
0.443	0.473	$3.70 \pm 0.12$	$1.11 \pm 0.06$	$1.72 \pm 0.15$
0.473	0.502	$3.63 \pm 0.12$	$1.02 \pm 0.06$	$1.53 \pm 0.12$
0.502	0.532	$3.64 \pm 0.12$	$1.04 \pm 0.06$	$1.68 \pm 0.14$
0.532	0.561	$3.82 \pm 0.12$	$1.10 \pm 0.05$	$1.91 \pm 0.16$
0.561	0.584	$4.78 \pm 0.15$	$1.19 \pm 0.05$	$2.38 \pm 0.21$
0.584	0.602	$6.21 \pm 0.18$	$1.06 \pm 0.05$	$2.31 \pm 0.18$
0.602	0.614	$9.26 \pm 0.26$	$1.02 \pm 0.04$	$2.47 \pm 0.18$
0.614	0.623	$12.67 \pm 0.35$	$1.05 \pm 0.04$	$2.85 \pm 0.22$
0.623	0.630	$15.16 \pm 0.41$	$1.09 \pm 0.04$	$3.01 \pm 0.24$
0.630	0.637	$16.50 \pm 0.44$	$1.03 \pm 0.04$	$2.73 \pm 0.20$
0.637	0.643	$17.78 \pm 0.48$	$1.08 \pm 0.04$	$2.88 \pm 0.22$
0.643	0.649	$17.88 \pm 0.48$	$1.13 \pm 0.04$	$3.24 \pm 0.26$
0.649	0.656	$15.89 \pm 0.44$	$1.10 \pm 0.04$	$2.66 \pm 0.21$
0.656	0.666	$11.74 \pm 0.33$	$1.13 \pm 0.04$	$2.89 \pm 0.23$
0.666	0.681	$8.14 \pm 0.24$	$1.26 \pm 0.04$	$2.91 \pm 0.26$
0.681	0.706	$4.67 \pm 0.15$	$1.32 \pm 0.05$	$2.83 \pm 0.30$
0.706	0.760	$1.94 \pm 0.07$	$1.30 \pm 0.06$	$1.86 \pm 0.20$
0.760	0.839	$1.18 \pm 0.05$	$1.42 \pm 0.07$	$1.79 \pm 0.23$
0.839	0.942	$0.83 \pm 0.04$	$1.44 \pm 0.09$	$1.30 \pm 0.19$
0.942	1.000	$0.81 \pm 0.06$	$1.48 \pm 0.17$	$0.87 \pm 0.19$

Table 3: Phase interval definitions and corresponding spectral parameters obtained from fitting the spectrum with a power law with exponential cut-off. The flux in the third column is normalized to the width of the phase bin. The systematic uncertainties are in agreement with the ones evaluated for the phase averaged analysis.

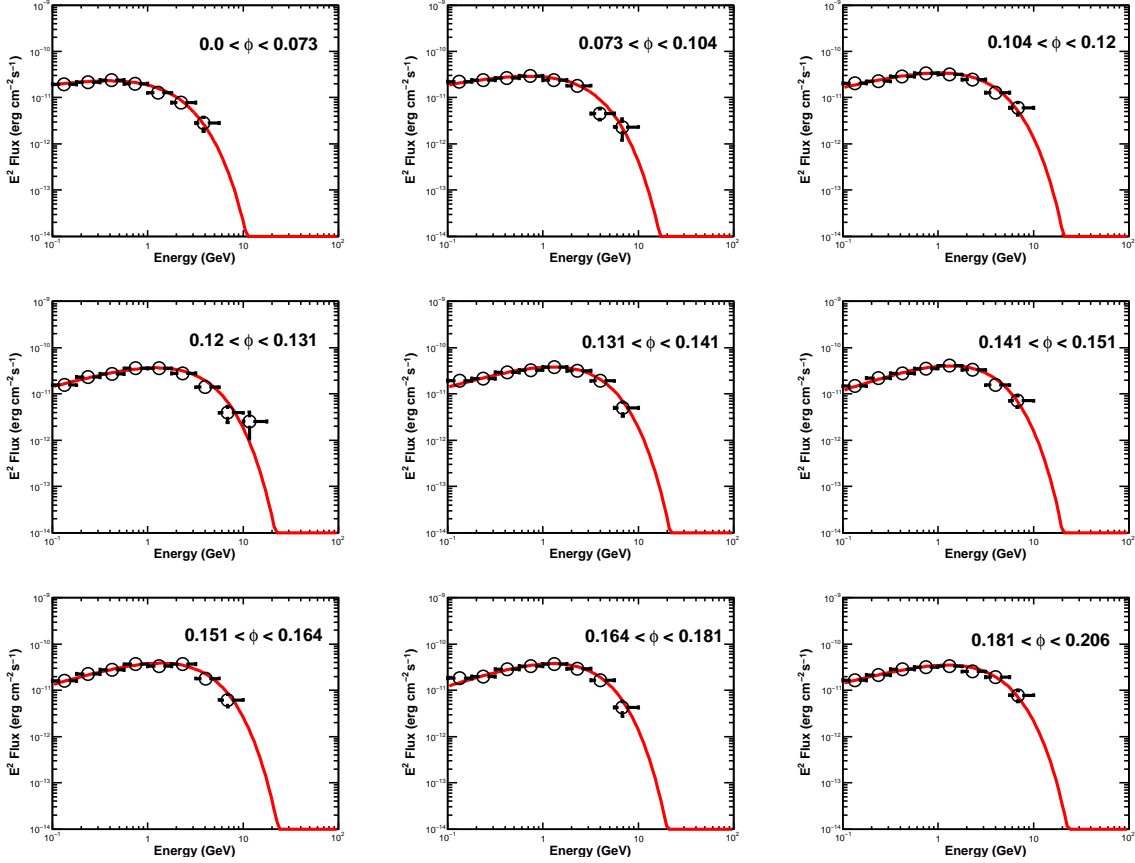


Fig. 9.— Phase-resolved Spectral Energy Distributions (SEDs) of the Geminga pulsar in the phase range  $\phi = 0.0 - 0.206$ . The spectral parameters of each of these spectral distributions can be found in Table 3. The fluxes are not normalized to the phase bin width, whereas in Table 3 the fluxes are normalized. The curves represent the best fit power law with exponential cut-off, while the LAT spectral points (open circles) are obtained using the maximum likelihood method described in Section 4.2

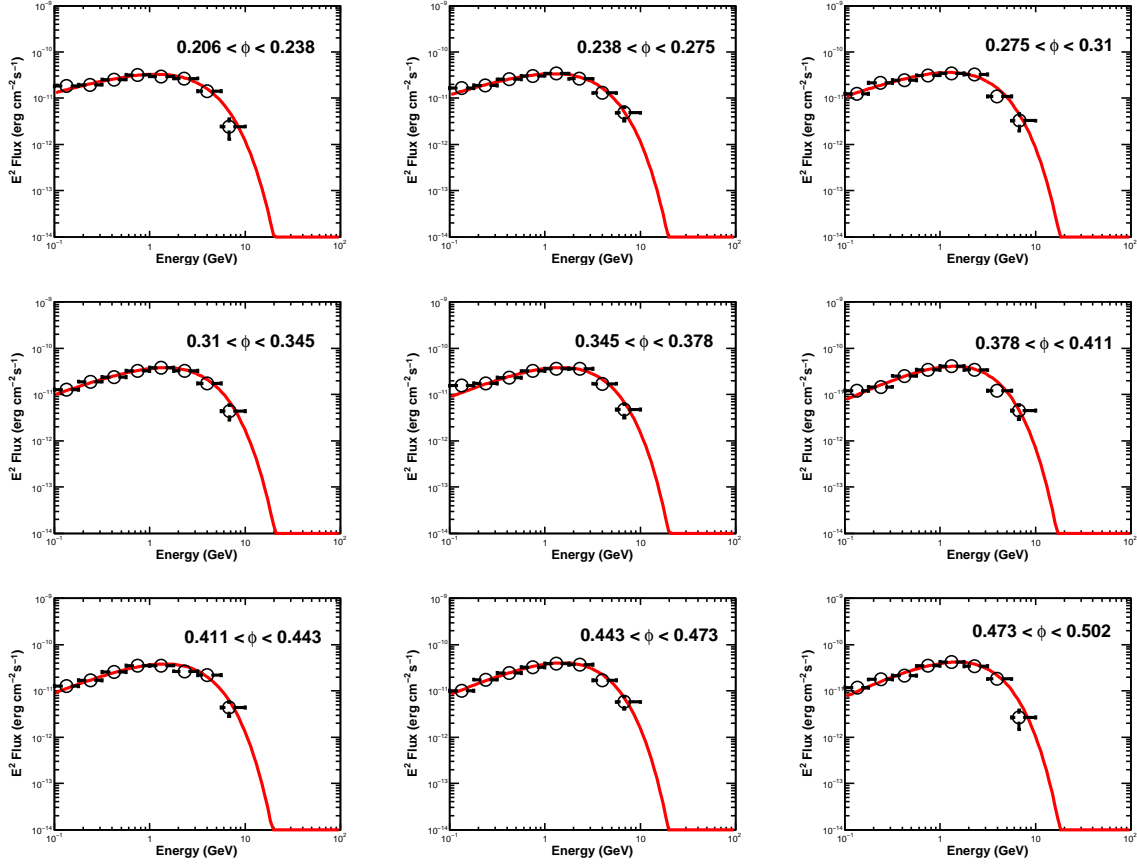


Fig. 10.— Phase-resolved Spectral Energy Distributions (SEDs) of the Geminga pulsar in the phase range  $\phi = 0.206 - 0.502$ .

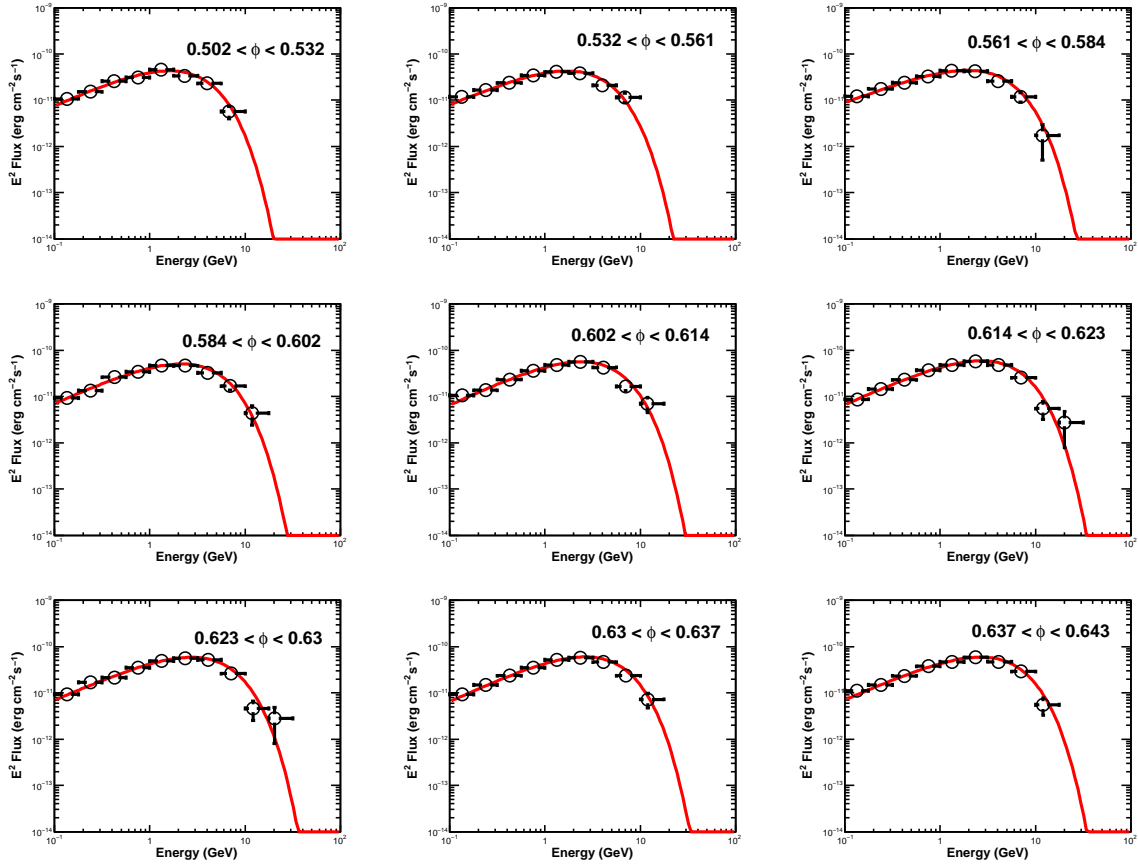


Fig. 11.— Phase-resolved Spectral Energy Distributions (SEDs) of the Geminga pulsar in the phase range  $\phi = 0.502 - 0.643$ .

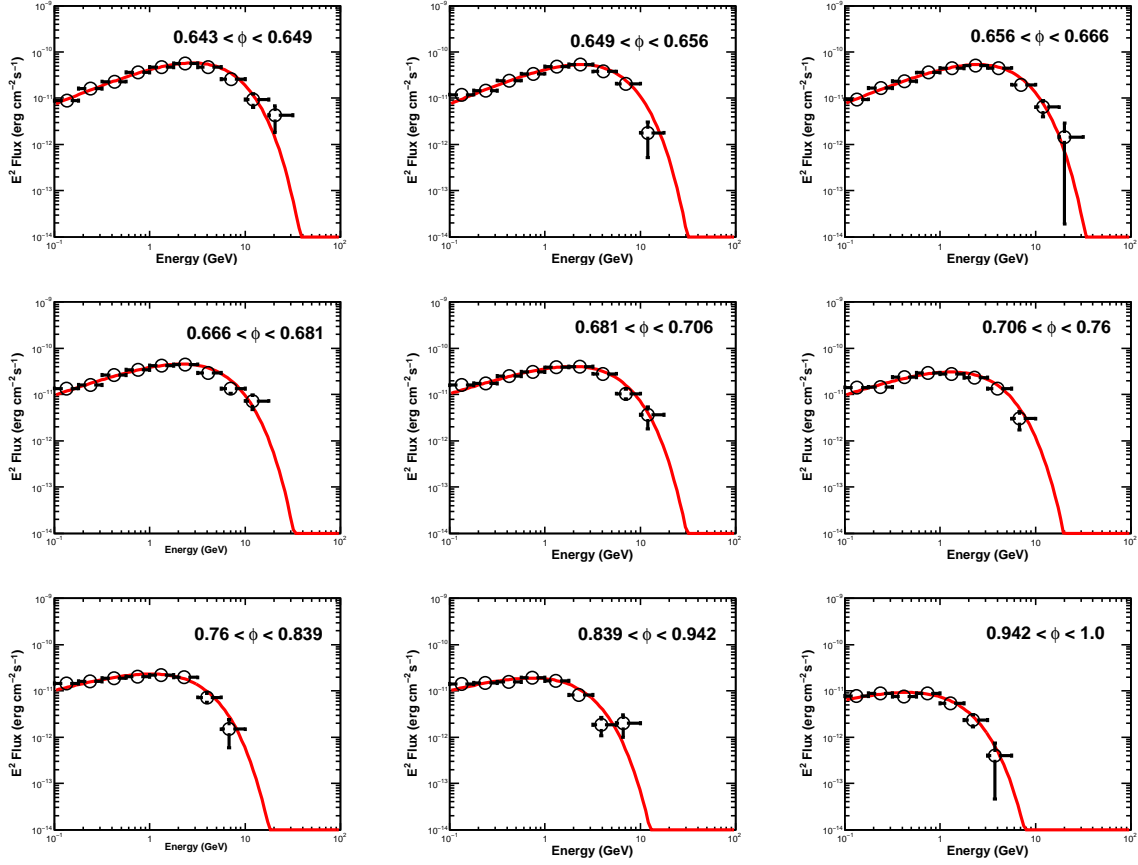


Fig. 12.— Phase-resolved Spectral Energy Distributions (SEDs) of the Geminga pulsar in the phase range  $\phi = 0.643 - 1.0$ .